The Effect of Orbital Radius and Stellar Mass on Gas Accretion in Giant Planet Formation

Brian Sheridan

MSc Thesis of Physics

Supervised by:
Prof. Dr. Ravit Helled
Dr. Sho Shibata
Prof. Dr. Sascha Quanz

September 9, 2024

Universität Zürich[UZH]

Abstract

It is commonly accepted that gas giant planets usually form through the core accretion model, where an initial solid core becomes massive enough to attract gaseous material, growing over time to form into a giant planet. However, the calculation of gas accretion rates in giant planet formation brings with it many uncertainties and often fails to explicitly account for the effects of the formation distance from the host star and host star mass itself. This thesis aims to investigate these effects on gas accretion rates. Firstly, initial observations are made from simulation data to investigate the change in gas accretion rates over these two parameters. Secondly, a new fitting function is developed to accurately and robustly calculate gas accretion rates, dependent on orbital radius and stellar mass. Finally, the fitted function is implemented computationally and used to gain insight into the formation of gas giant planets. The findings elucidate features of gas accretion rates, as well as a useful new variable over which to fit gas accretion rate functions, namely the envelope mass multiplied by the solid accretion rate. It is found that the crossover mass leading to runaway gas accretion is robustly reached within the disk lifetime for stellar masses above a value of approximately half a solar mass, below which the timescales extend too long. We also see that this timescale correlates with the total planet mass at the onset of rapid gas accretion, and that planets with total mass approximately equal to or less than 40 Earth masses at the onset of rapid gas accretion do not reach crossover mass within the disk lifetime. These insights pave the way for future work.

Acknowledgements

This Master's thesis represents the culmination of a long journey with physics. It has been a privilege to work on a truly fascinating topic in astrophysics over the course of six months and I would like to thank the people involved in this capstone project of my physics education.

I would like to begin by thanking Prof. Dr. Ravit Helled for the opportunity to be part of her research group and to perform my Master's thesis there. It is greatly appreciated and I really enjoyed the experience. I would like to thank her for her generosity and entrusting me with researching a fascinating and relevant topic in planetary science.

I would also like to thank Dr. Sho Shibata for his irreplaceable guidance, helping me to navigate a new field of physics, become familiar with new simulation software and to answer my numerous questions on astrophysics. His patience was greatly appreciated and his joy of physics greatly admired.

I would like to thank Dr. Simon Müller for the pleasant conversations we had and the numerous insights he provided throughout the course of this project. The insightful discourse acted as valued support during the latter stages of the thesis.

Lastly, I would like to thank my friends, family and those close to me for the support given during this thesis project. Their unwavering support and positivity will always be cherished.

"The nitrogen in our DNA, the calcium in our teeth, the iron in our blood, the carbon in our apple pies were made in the interiors of collapsing stars. We are made of starstuff."
- Carl Sagan, Cosmos

Contents

1 Introduction

An interest in planets dates far back in human society, with the term *planet* deriving from the ancient Greek word for "wandering star", given their apparent movement against a fixed background of stars. For much of society's history the understanding of planets was restricted to observations of solar system planets, with terrestrial planets, gas giant planets and ice giant planets comprising the classic architecture of planetary classifications. A major advancement came in the year 1992 when the first *extrasolar planet*, or exoplanet, was discovered, a planet orbiting around another star [1]. This opened the floodgates for more exoplanets to be discovered and, with it, a myriad of observed and possible planetary types, such as super-Earths, sub-Neptunes, hot Jupiters or even more theoretical planetary models such as hycean planets. These manifold planetary possibilities challenge our understanding of how planets are formed. Figure 2 shows a selection of discovered exoplanets using three main detection techniques. Many discovered exoplanets indicate large masses of hundreds of Earth masses.

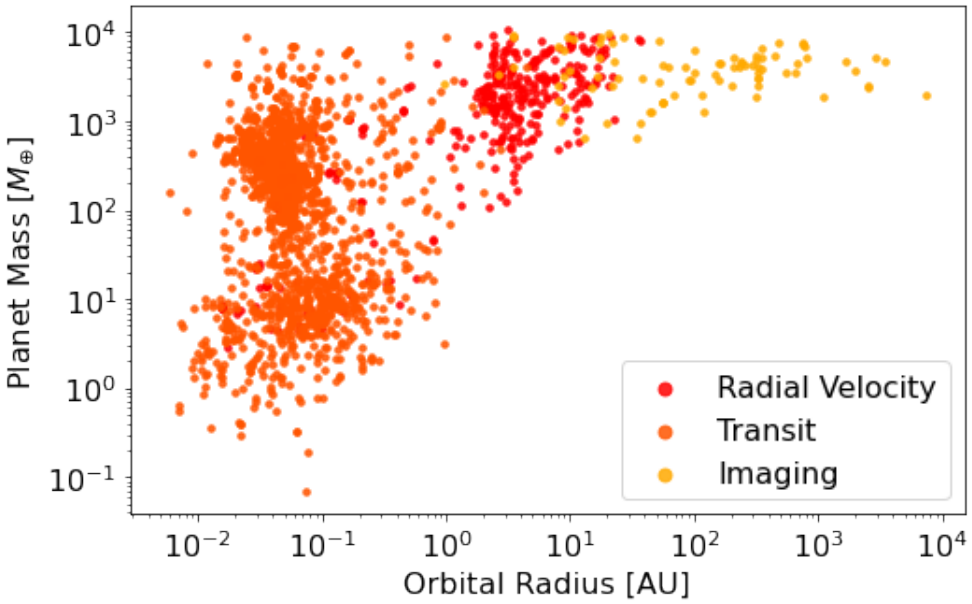

Figure 2: A selection of discovered exoplanets using three main detection techniques, namely the radial velocity, transit and direct imaging techniques.

Gas giant planets are a particular planetary class of interest, given their massive size, their combination of gaseous material and solid material and the high number of giant exoplanet detections. The gas giant planets contrast with terrestrial planets without a significant gaseous envelope and offer valuable insight into how forming planets interact with the solar nebula. These planets exert a huge gravitational influence and can even play a role in the dynamics of an evolving stellar system. A prominent example of the role of gas giants in planetary dynamics is that of the *Nice model* [2]. This model proposes that the architecture of the solar system was different during early formation, however the gravitational exertion of the early gas giants of Jupiter and Saturn caused other planets to migrate outward and lie

today at an orbital separation further away from the sun. This is only one example of how gas giants are both interesting and essential to our understanding of planetary formation and exoplanet observations. The contrasting inclusion of copious amounts of gas, as compared to less massive astrophysical bodies, naturally poses the question of how a planet can form with such a copious amount of gas.

The *core accretion* model is a commonly accepted model of planetary formation, stipulating that planets grow iteratively and gradually over time. At a certain point, the gravitational strength of a forming planet is large enough to attract gas from its vicinity and begins to form a gaseous envelope. The rate at which gas is accumulated is, however, poorly understood. This reduces the accuracy of gas accretion rate calculations, therefore limiting our investigations into the growth of gas giant planets. Often neglected in these calculations of gas accretion rates are the effects of orbital separation from the host star and the mass of the host star itself. These parameters can affect the rate at which gas is accreted onto a planet. Investigating the effects of these parameters on gas accretion rates allows us to improve the accuracy of the calculation of gas accretion rates and gives us further insight into the physical mechanisms involved with gas accretion.

The goal of this thesis is to investigate the effects of orbital separation and host star mass on gas accretion rates. We also wish to improve the quality of predicting gas accretion rates by proposing new methods of calculation which are both robust and accurate. Finally, we wish to use our results to investigate aspects of giant planet formation.

2 Theory

The formation of planets occurs as a consequence of the formation of stars. Star formation results from the collapse of molecular clouds, which are cold, dense clouds of gas and dust, representing regions of overdensity in the galaxy [3]. These clouds are in hydrostatic equilibrium, meaning that the gravitational and pressure forces balance each other. For systems in gravitational equilibrium, we can apply the virial theorem, given as

$$2E_{\text{Kin}} + E_{\text{Pot}} = 0\,, \tag{1}$$

in order to calculate the mass needed for an equilibrium state. Upon substituting the kinetic energy for molecular thermal energy, the potential energy with gravitational energy and assuming a homogeneous sphere, we obtain the *Jeans mass*,

$$M_J = \left(\frac{375}{4\pi}\right)^{1/2} \left(\frac{k_B}{G\mu}\right)^{3/2} \frac{T^{3/2}}{\rho^{1/2}}\,. \tag{2}$$

This is the critical mass beyond which the gravitational force dominates over the thermal pressure. Note that it is for a given density, ρ, meaning that if we increase the density the value of the critical mass decreases. Given a molecular cloud with a mass just at the Jeans mass, any physical phenomenon which compresses the cloud and increases the density would result in a gravitational collapse. If contracting isothermally, these clouds can fragment into

smaller clouds, since the density would increase, reducing the critical Jeans mass and thus promoting collapse in different regions within the cloud. This would lead to the collapse of the cloud into multiple distinct subclouds.

These large molecular clouds possess a lot of angular momentum. Although slowly rotating, the large value of angular momentum is hidden in the large size of the molecular cloud. As the cloud shrinks, conservation of angular momentum makes the constituent fragments speed up their rotation. Combining the gravitational collapse with the conservation of angular momentum eventually results in the formation of a protostar surrounded by a circumstellar disk, with the protostar holding most of the mass but the circumstellar disk holding most of the angular momentum. In our solar system, for example, the sun holds more than 99 percent of the entire mass of the solar system, however roughly 99 percent of the angular momentum is held by the planets, with the angular momentum of Jupiter being almost 100 times larger than that of the sun, suggesting a strong separation of angular momentum in the solar system [4]. The disk surrounding the young protostar is a collection of gas and dust which eventually vertically settles into a thin disk, acting as the cradle of planet formation. Eventually after a few million years, the circumstellar disk disperses, defining an end to the supply of material for planetary formation and an end to the main planetary formation phase, excluding dynamical evolution after the disk dispersal.

The estimation of circumstellar disk lifetimes is primarily obtained from observations of the dust in the disk. Dust particles absorb and reradiate infrared light and are much easier to observe than the gas. Data from the *Spitzer* mission and related observations have indicated a median disk age of 2 and 3 million years, with the age of some disks up to 10 million years [5]. After this time, the disk begins to disperse. The constant accretion into the host star removes disk material in the inner region, while viscous evolution and photoevaporation push disk material in the outer region out of the vicinity of the host star and the planet forming region. Giant planets, and planets in general, must form within this time. Once the disk disperses, there exists no more supply of gas or solid material to contribute to growth.

Leading on from the genesis of the protostar and the corresponding circumstellar disk, the following sections outline the physical models and processes relevant for the formation of gas giant planets.

2.1 Gas Disk Models

The disk which encompasses a young star comprises a range of material types. We can decompose the disk into its constituent parts based on composition and conceptually define the portion of the disk composed primarily of hydrogen and helium as the *gas disk* [6]. The composition of the circumstellar disk reflects the composition of the host star, meaning that the gas disk comprises the dominant mass fraction of the whole disk, just like the host star. The mass fractions for stellar composition can be defined as $X + Y + Z = 1$ where, X, Y and Z are the mass fractions of hydrogen, helium and solids, respectively. For the sun these are taken approximately to be $X = 0.74$, $Y = 0.25$ and $Z = 0.01$ [7], which are normally

reflected by the circumstellar disk. The behaviour of the gas disk is influenced by the host star and the forming planets, with features such as accretion onto the host star, spiral waves through the disk and pressure bumps in the disk. The gas disk in turn influences the growth of planets, including their mass evolution as well as their dynamical evolution. There are a variety of different mathematical models to describe gas disks, with different models chosen for different conditions and problems. The theory of these gas disks is outlined below, while further details can be found in Armitage (2020) [8].

2.1.1 Vertical Structure

Analysis of the general vertical structure of a gas disk gives insight into its density profile. The density profile is important since it dictates the amount of gaseous mass available to a planet during formation as well as affecting the dynamical evolution of the planets. Consider a young circumstellar disk surrounding a protostar, as depicted in figure 3.

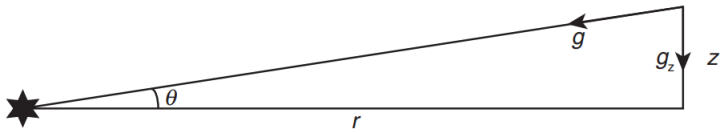

Figure 3: Splitting the gravitational force on the gas disk into components. Adapted from Armitage (2020) [8].

The vertical gravitational component is given as

$$g_z = g \sin\theta = \frac{GM_*}{(r^2+z^2)} \frac{z}{(r^2+z^2)^{1/2}}, \tag{3}$$

which must balance the vertical pressure gradient acceleration in the gas, namely

$$\frac{1}{\rho}\frac{dP}{dz}.$$

Assuming an ideal gas law, meaning $P = \rho c_s^2$, we get

$$c_s^2 \frac{d\rho}{dz} = -\frac{GM_* z}{(r^2+z^2)^{3/2}}\rho,$$

which, when assuming a thin disk, $z \ll r$, and the Keplerian $g_z \simeq \Omega^2 z$, where

$$\Omega = \sqrt{GM_*/r^3}, \tag{4}$$

gives the solution

$$\rho = \rho_0 e^{-z^2/2H^2}, \quad \rho_0 = \frac{1}{\sqrt{2\pi}}\frac{\Sigma}{H}, \tag{5}$$

where ρ_0 is the midplane density, Σ is the gas surface density

$$\Sigma = \int_{-\infty}^{+\infty} \rho_0 \exp\left(\frac{-z^2}{2H^2}\right) dz\,, \tag{6}$$

and

$$H = \frac{c_s}{\Omega}, \tag{7}$$

is the vertical disk scale height. The speed of sound in the disk is related to the microscopic thermal properties of the disk and, given the ideal gas law, is defined as the isothermal sound speed, namely

$$c_s^2 = \frac{k_B T}{\mu m_p}. \tag{8}$$

This analysis allows us to understand the general structure of the gas disk in terms of the change in density vertically at a given point in the disk. However, to understand the profile of the disk and how it changes with orbital radius from the host star and with time, we need to understand how mass and angular momentum behave within the disk.

2.1.2 Viscous Gas Disks

The profile of a gas disk may be characterised by its surface density,

$$\Sigma = \Sigma(r,t) = \int_{-\infty}^{\infty} \rho(r,t,z) dz. \tag{9}$$

This is an evolving quantity, with the most basic dependencies spanning over radius and time, in the case of a one-dimensional disk. In order to compute this quantity for a given radius and time, one needs to know how to profile evolves over these two dimensions. In other words, one needs to determine how angular momentum and mass are transferred throughout the disk. This central question was tackled by the likes of Shakura and Sunyaev (1973) [9] and Linden-Bell and Pringle (1974) [10], with the main details covered here.

In order to arrive at the relevant equations describing the gas disk surface density, we need to consider the conservation of angular momentum and the conservation of mass. We can firstly focus on the conservation of angular momentum. If we consider the rate of change of mass in an annulus extending from r to Δr, we find

$$\frac{\partial}{\partial t}\left(2\pi r \Delta r \Sigma\right) = 2\pi r \Sigma(r) v_r(r) - 2\pi(r+\Delta r)\Sigma(r+\Delta r) v_r(r+\Delta r).$$

Extending the analysis as in Pringle (1981) [11], we understand that the quantity $2\pi r \Delta r \Sigma$ represents the amount of mass in the annulus between r and Δ, and that the angular momentum of this mass is $2\pi r \Delta r \Sigma r^2 \Omega$, we can multiply our equation by $r^2\Omega$ and then take the limit as $\Delta r \to 0$ to find

$$r\frac{\partial(\Sigma r^2 \Omega)}{\partial t} + \frac{\partial}{\partial r}\left(r \Sigma v_r r^2 \Omega\right) = \frac{1}{2\pi}\frac{\partial G}{\partial r}.$$

The term on the right hand side comes from viscous torques in the disk from the annuli around the given annulus, with the torque given by the quantity G. The torque on an annulus is caused by the shearing with other neighbouring annuli, described by the shearing rate

$$A = r\frac{d\Omega}{dr},$$

with units of radians per second. Given that the definition of torque is the force applied times the distance and generalising over the entire disk, the torque can be written as

$$G = 2\pi r\nu\Sigma A = 2\pi r\nu\Sigma r\frac{d\Omega}{dr},$$

where the kinematic viscosity, ν, has been introduced here, which describes the internal friction within the disk [5].

Performing a similar analysis on the conservation of mass, where we do not multiple our equation by $r^2\Omega$ to achieve angular momentum, we arrive at our two conservation equations,

$$\frac{\partial(r^2\Sigma\Omega)}{\partial t} + \frac{1}{r}\left(\Sigma v_r r^3\Omega\right) = \frac{1}{r}\frac{\partial}{\partial r}\left(\nu\Sigma r^3\frac{\partial\Omega}{\partial r}\right), \tag{10}$$

$$\frac{\partial\Sigma}{\partial t} + \frac{1}{r}\frac{\partial}{\partial r}\left(r\Sigma v_r\right) = 0. \tag{11}$$

Substituting the mass conservation equation into the first equation, for angular momentum conservation, and assuming the orbital frequency, Ω, is Keplerian, we finally obtain

$$\frac{\partial\Sigma}{\partial t} = \frac{3}{r}\frac{\partial}{\partial r}\left(\sqrt{r}\frac{\partial}{\partial r}(\nu\Sigma\sqrt{r})\right). \tag{12}$$

There exist different solutions to equation (12), although one pertinent solution relies on the assumption that the viscosity can be described as a power law in the radius,

$$\nu \propto r^{\gamma}, \tag{13}$$

which gives the *self-similar solution*, first proposed by Lynden-Bell and Pringle in 1974 [10]. We assume that at time $t = 0$ the solution is the steady-state solution up to a cutoff radius $r = r_{\text{out}}$, beyond which there entails an exponential decrease. Once we take time evolution into account, our self-similar solution is then given as

$$\Sigma\left(r,t\right) = \frac{\dot{M}_{0,\text{disk}}}{3\pi\nu_{\text{out}}(r/r_{\text{out}})^{\gamma}}T_{\text{out}}^{-(5/2-\gamma)/(2-\gamma)}\exp\left[-\frac{(r/r_{\text{out}})^{2-\gamma}}{T_{\text{out}}}\right], \tag{14}$$

where the quantity $\dot{M}_{0,\text{disk}}$ describes the gas accretion rate from the disk onto the host star and γ is the radial viscosity gradient. The function T_{out} is a function of time and is given as

$$T_{\text{out}} = 1 + t/t_s\,, \tag{15}$$

where

$$t_s = \frac{1}{3\left[2-\gamma\right]^2}\frac{r_{\text{out}}^2}{\nu_{\text{out}}}\,. \tag{16}$$

The surface density profile is shown in figure 4 as functions of both orbital separation and time for a solar mass star. The solution decreases in a power law fashion with an exponentially tapered cutoff at radii comparable to the outer cutoff radius.

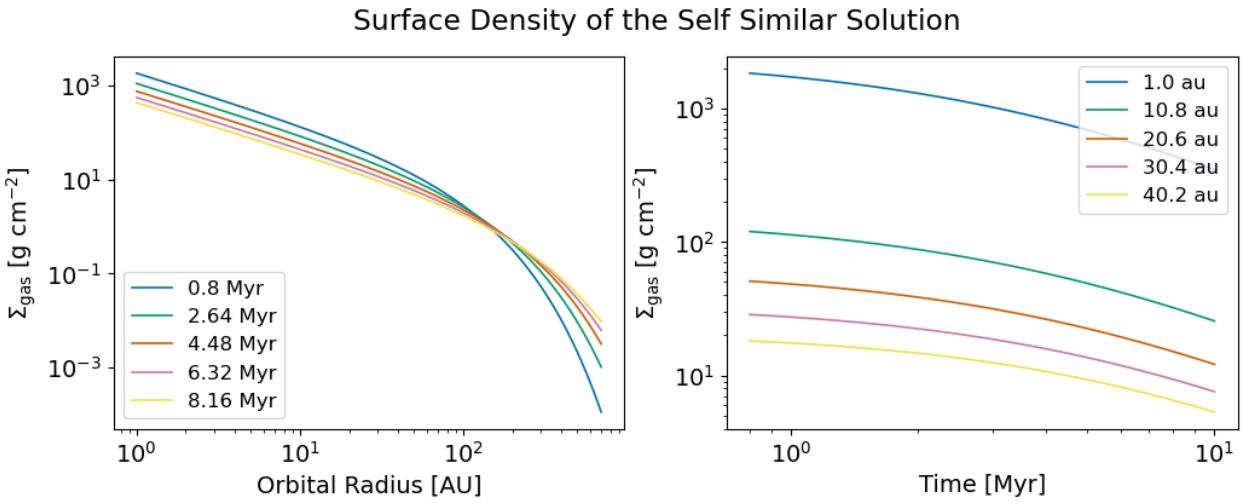

Figure 4: The gas disk surface density over orbital radius and over time for a star of one solar mass. The self-similar equation is used.

One issue with the above analysis on accretion disks is that there is no explicit description of the efficiency at which angular momentum is transported through the disk, or more details on angular momentum transport in general. Attempts were made by Shakura and Sunyaev to resolve this caveat by introducing the α-disk model [9]. The strength of molecular viscosity was noted as being a negligible factor contributing to the overall viscosity, leading to the idea that *turbulence* is the main source of viscosity. The α-disk model stipulates that turbulence in the disk creates eddies, with an upper size limit corresponding to the scale height of the disk, which can provide an effective viscosity much stronger than molecular viscosity. This turbulence thus acts as the main factor in the calculation of the viscosity. This kinematic viscosity caused by turbulent eddies is calculated as

$$\nu = \alpha c_s H = \alpha \Omega_K H^2 \,, \tag{17}$$

where α is a dimensionless measure of how efficiently angular momentum is transported through the disk, given that turbulence is the underlying mechanism.

2.2 Solid Disk Models

Along with the gaseous component of the protoplanetary disk, there also includes a component of solid material. This can be coined as the *solid disk* and consists of substances which are neither hydrogen nor helium. This includes rock (silicates), volatiles and water, among other substances. The ratio of solid material to gaseous material is called the metallicity, usually around a value of 0.01, again reflecting the stellar composition. The metallicity thus

gives an indication of the amount of solid material available for planetary formation. Initially, solids are in the form of dust particles, which are small particles on the order of a few micrometers, usually porous and well coupled to the gas. These dust particles follow from the molecular cloud and the initial circumstellar disk formation. These dust particles then collect into larger structures through a variety of physical mechanisms, with solid material sizes increasing in 12 orders of magnitude as they evolve from tiny dust particles to planets. The analysis of meteorites provides us with much of the information needed to ascertain the composition and behaviour of solid material in the early protoplanetary disk. A special class of meteorites which are of particular importance are chondritic meteorites, which are undifferentiated bodies, meaning that they never became hot enough for substances to separate within the body and form a distinct layered structure. These objects would have formed directly from the protoplanetary disk and have a bulk composition similar to the sun. Radioactive dating can place an age on these meteorites, which formed pristinely from the early solar nebula, giving an age of approximately 4.567 billion years, conventionally known as the age of the solar system [12].

There are different regimes for the growth of solid material. Due to the enormous increase in sizes over time, different physical effects take hold during different phases of the growth and therefore the different phases may be treated separately. These different phases can be categorised by the scale of the solids. A rough categorisation proceeds as follows [8].

1. **Dust:** The earliest stage of solid material collections are dust particles, with sizes on the order of micrometers to up to a centimetre and are well coupled to the gas. Growth out of this stage occurs from collisions.

2. **Rocks/Pebbles:** Rocky material is on the order a meter and is weakly coupled to the gas, meaning it experiences a drag force from the gas throughout the orbit. The growth mechanism is not entirely clear at this point, as collisions which are too rapid can lead to fragmentation. The growth out of this stage is, however, found to be quick.

3. **Planetesimals:** The objects are on the order of 1 kilometer in scale and are decoupled from the gas. These bodies are massive enough to start exerting a gravitational pull, enhancing their growth, and they are mostly decoupled from the gas.

4. **Embryos:** Once a collection of solid material reaches a scale size of around 1000 kilometers it can be considered a planetary embryo, which is the progenitor of a planet. This scale can extend all the way to Earth sized masses as planets. The gravitational strength at this size is now large enough to couple the body to the gas again, which can induce effects such as gas accretion or planetary migration from interactions with the disk.

5. **Planetary Cores:** These objects are larger than the Earth, on the order of about 10 Earth masses, and are the cores of giant planets in the core accretion model. These mark the transition point from hydrostatic growth to faster runaway growth of giant planets and rapid gas accretion.

As mentioned, different mechanisms promoting the growth of solids occur at different phases, where gas disk interactions, collisions or gravitational interactions becoming more or less important for different masses of solids. It is important to understand these different solid accretion mechanisms in order to understand the growth of solids and gas into giant planets.

2.2.1 Solid Accretion

The initial growth from dust to planetesimals may be driven by numerous factors. After the formation of the circumstellar disk, the dust gradually settles to the midplane due to the vertical component of the gravitational interaction with the star acting towards the midplane. As the dust particles move toward the midplane, they collide with other dust particles and stick together to make larger particles, in a process known as *coagulation*. These collisions may also be exacerbated by radial drift and other random collisions which lead to particle growth. There may also exist strong turbulence in the disk, which may oppose the settling force towards the midplane, meaning that substantial particle growth needs to occur to accrue enough mass in order to counteract turbulent forces before the particles fully settle to the midplane [6]. The strength of this coagulation process increases beyond the ice line, since the relative speeds between two particles, below which they still stick after a collision, increases significantly in the presence of ice.

Difficulties, however, persist in this model of solid material growth. Once particle sizes become big enough, particle collisions may lead to fragmentation and therefore the reduction of particle sizes. The presence of ice beyond the ice line mitigates this effect although it is still relevant, especially for objects closer to the host star. This presents an inhibiting factor in the growth of particles from dust and rocks to planetesimals. Additional mechanisms have been proposed to explain the rapid growth of planetesimals. One such idea is the *Goldreich-Ward* mechanism, which proposes the accretion of solid material as a result from a gravitational instability within the disk [13]. Given a combination of vertical settling and radial drift, the local density of solid material may become higher than the local density of gas, meaning that the solid disk fragments into clumps due to a gravitational collapse. These clumps dissipate energy through collisions and form planetesimals.

The criterion for an instability leading to collapse into planetesimals is described by the Toomre parameter, explained later in section 2.3.1, and requires the disk to be cool and dense. These conditions are often hard to meet, meaning that the additional effect of *streaming instabilities* becomes relevant, which promotes overdensities of solid material in the disk to form [8] [14]. These instabilities occur in Keplerian disks with aerodynamically coupled mixtures of gas and particles. On long enough timescales, we can treat the disk as a fluid and analyse the collective motion. The fluid motion of the disk can result in filaments composed of overdensities of solids, leading to non-gravitational collapse.

The full process leading to the formation of planetesimals is still not fully understood, although the described mechanisms constitute the leading ideas for growth beyond scales of approximately a meter. Growth beyond the planetesimal scale is also treated qualitatively

differently and introduces further physical mechanisms for growth. At this scale, larger solid material becomes massive enough to exert a gravitational influence on neighbouring solids. Collisions present less of an issue since fragmented solids can remain gravitationally bound and coalesce into each other. Additionally, gravitational focussing provides a method of expanding the radius of accretion. Instead of the physical size of the solid material being the radius of solid accretion due to collisional interactions with other solids, there exists a gravitational influence which increases the reach of influence that the solid material has. A conceptually simple equation describing *planetesimal driven solid accretion* from Safranov (1969) [15] may be given as

$$\frac{dM_{\text{solid}}}{dt} = \pi R_{\text{capt}}^2 \Sigma_{\text{solid}} \Omega F_g, \tag{18}$$

with πR_{capt} the geometric cross section, Σ_{solid} the solid disk surface density, Ω the orbital frequency and

$$F_g = \left[1 + \left(\frac{v_e}{v}\right)^2\right], \tag{19}$$

the gravitational focussing factor, which acts to amplify the effective radius of accretion the larger the mass is, given an escape velocity v_e and relative velocity of solid bodies v. This focussing factor is only relevant in a two-body problem approximation, where stronger effects from the host star make the form of the focussing factor more complicated.

2.2.2 Pebble Accretion

Solid material growth driven by planetesimal accretion brings with it a few problems. Planetesimal accretion is only efficient if the planetesimals are small, less than 100 kilometers in diameter [16]. This means that the timescale for solid mass growth increases as the efficiency decreases, and the timescales for planetary growth come into conflict with the protoplanetary disk lifetimes. Also, planetesimal driven growth relies on the assumption that all smaller solids have been cleared from the disk and turned into planetesimals. This assumption is not necessarily true and smaller solids can still exist, which interact aerodynamically with the gas disk, leading to enhanced solid accretion [8]. Planetesimal formation is also a poorly understood concept with issues such as the meter-sized-barrier, where there exist issues conceptualising how the solids grow beyond this approximate size. These flaws necessitate the introduction of a new solid accretion method, namely *pebble accretion* [17] [18].

Once solid materials reach the size of planetesimals they are mostly decoupled from the gas and only impact another solid body due to a direct collision or a gravitationally assisted collision. Pebbles are smaller solids which are still coupled to the gas. This means that both gravitational and aerodynamic drag forces are experienced by the pebble in the presence of a larger solid body. The addition of aerodynamic drag enhances the collisional cross section of the massive solid body and allows it to accrete more solid material. The diagrams shown in figure 5 illustrate the difference between pebble and planetesimal accretion. The left hand diagram shows the effect of pebble accretion making passing trajectories fall into the growing solid body, since aerodynamic drag acts in tandem with gravitational focussing in order to enhance the solid accretion rate. The right hand diagram shows the effect of planetesimal

Figure 5: The cross section for capture is enhanced with pebble accretion, in the left hand diagram, as opposed to solely planetesimal accretion, in the right hand diagram. The aerodynamic drag in combination with gravitational focussing leads to higher solid accretion rates. The central filled dot represents a growing solid body and the dotted circle around it is the Hill radius, outlining the region of gravitational influence. The grey filling only indicates that pebble accretion is being taken into account in the given diagram. The trajectories for solid particles can fall into the planet due to aerodynamic drag, whereas the same trajectories pass by the planet when no aerodynamic drag is taken into account.

accretion, where only gravitational focusing is included and the effects of aerodynamic drag ignored.

The pebble accretion rates can be solved analytically and are presented in Lyra et al. (2023) [19]. Focussing on the monodisperse solution, where the solid particles are taken to assume a single size, we see the solid accretion rate as

$$\dot{M}_{\rm pe} = \pi R_{\rm acc}^2 \rho_{\rm pe} \delta v \exp(-\xi) \left[I_0(\xi) + I_1(\xi) \right] , \tag{20}$$

where

$$\xi = \left(\frac{R_{\rm acc}}{2H_{\rm pe}} \right)^2 , \tag{21}$$

and I_ν are modified Bessel functions of the first kind. The quantity

$$\begin{aligned} S &= \frac{1}{\pi R_{\rm acc}^2} \int_{-R_{\rm acc}}^{R_{\rm acc}} 2\sqrt{R_{\rm acc}^2 - z^2} \exp\left(-\frac{z^2}{2H_d^2} \right) dz \, , \\ &= \exp(-\xi) \left[I_0(\xi) + I_1(\xi) \right] , \end{aligned} \tag{22}$$

is the stratification integral, which integrates over infinitesimally thin horizontal chords within a sphere the size of the accretion radius, extending above and below the midplane, weighted by the value of an exponential function measuring the decay of the material density in the vertical direction. The full set of equations for pebble accretion is given in the Appendix.

The pebble accretion rate exhibits a decay over orbital radius in a fashion similar to a power law. This can be seen in figure 6 where the pebble accretion rate from equation (20) is plotted over orbital radius from a solar mass star and a star of 0.6 solar masses, for different cases of a planet mass. The efficiency of pebble accretion reduces significantly over orbital radius, indicating a significant dependency on the separation from the host star. The pebble accretion rate also decreases with a decrease in the host star mass.

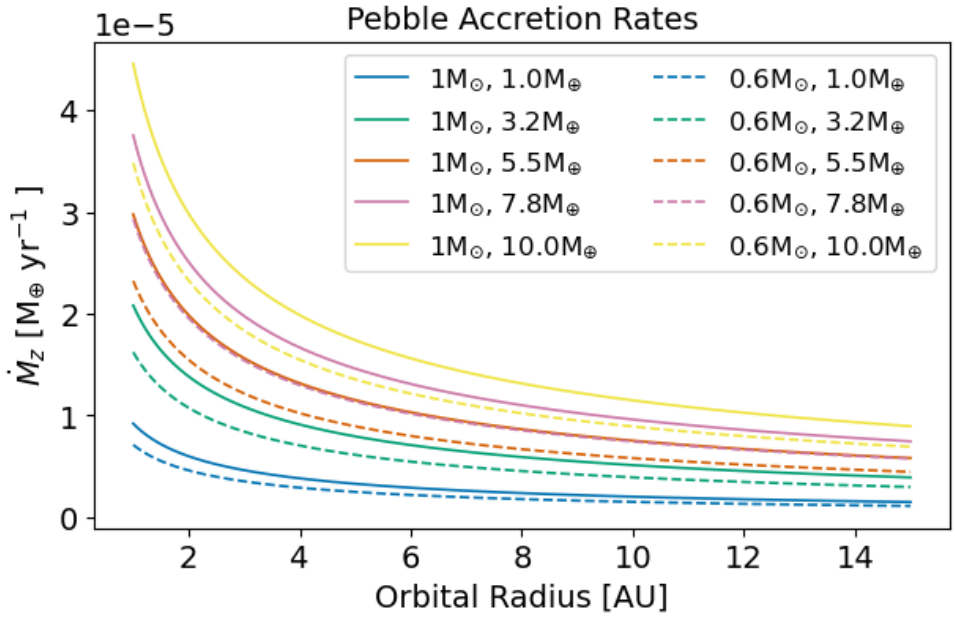

Figure 6: Pebble accretion rates for multiple planet masses for a solar mass star and a star of 0.6 solar masses.

2.3 Giant Planet Formation Theories

Planetary growth occurs from an accumulation of material by gravitational attraction and by other physical mechanisms. The solid accretion pathways of planetesimal and pebble accretion offer ways in which solid material can accumulate into larger bodies and planetary embryos within the protoplanetary disk. In order to form gas giant planets, however, there need to exist efficient mechanisms to accumulate large amounts of gas along with solids. This stems from analysis of solar system planet interiors showing that hydrogen and helium comprise the dominant mass fraction of gas giants, along with a certain mass of solid material. How do planets accumulate gas from the protoplanetary disk and how is this done efficiently such that the dominant mass fraction of planets can be hydrogen and helium?

There are two main theories to explain the origin of gas giants. The first is the *core accretion* model which postulates that an initial mass of solids accumulates through solid accretion mechanisms. The gas accretion rate for low masses is low but raises to significant levels once the mass of the planetary embryo becomes large enough, at which point gas is gradually accreted and an envelope begins forming. The gas accretion rate increases gradually until approximately the *crossover mass* is reached, when the solid and gaseous masses are approximately equal, at which point the gas accretion rate increases sharply and the growing planet can accumulate vast quantities of gas. The result is a gas giant planet with a core of heavy elements and a significant envelope of gaseous material.

The second theory is the *disk instability* model. It was proposed as an alternative mechanism to core accretion for forming giant planets [20]. In this model, we assume that filaments can form in the circumstellar disk, which represent an overdensity of solid material compared

to gaseous material. Given certain criteria, these local regions are prone to gravitationally induced collapse, bringing together vast amounts of gaseous and solid material together to form gas giants. The timescales involved with the disk instability model are very short, which offer a solution to the longer timescales of core accretion. However, the criteria for disk instability are difficult to achieve, presenting some obstacles to its general acceptance.

We start with an introduction to disk instability before providing an overview of the more commonly accepted core accretion model.

2.3.1 Disk Instability

One theory for the growth of giant planets is the disk instability model. This relies on the idea of a circumstellar disk being unstable to gravitational collapse, given certain conditions. The ideas for the analysis of instability in circumstellar disks were first expounded upon by Safranov in 1969 [21], however a more complete analysis was proposed by Toomre in 1964 [22]. Considering an axisymmetric circumstellar disk, the criterion for collapse depends on the gravitational force promoting collapse overwhelming the thermal pressure of the disk promoting stability.

The relevant equation describing the collapse criterion is then given as

$$Q = \frac{c_s \Omega}{\pi G \Sigma} < Q_{\text{crit}} \simeq 1, \tag{23}$$

where the *Toomre parameter*, Q, has been introduced. If this value is less than unity, the disk is prone to gravitational collapse, otherwise it is stable. We can see that the factors which decrease the value of Q, and thus promote collapse, are a denser disk, a cooler disk (since the sound speed is proportional to the square root of the temperature) and a location further from the star which results in a lower orbital frequency. The surface density, however, decreases the further away from the star one is, even though the temperature and orbital frequency also decrease, suggesting an interplay between the parameters which warrants computational treatment.

Although the disk instability model was proposed as an alternative to the more widely accepted core accretion mode, it does not come without its caveats. The Toomre criterion for gravitational collapse in equation (23) shows that the disk must be massive and/or cold. These criteria are not always easily met and depend on the system at hand. Often times, hydrodynamic arguments are invoked in order to provide an explanation for the initial formation of clumps in order to trigger gravitational collapse. Treating the circumstellar disk as a fluid on long enough timescales, we can point to *streaming instabilities* as a possible method of perturbing a region of the disk into an overdensity, the same streaming instabilities of section 2.2.1, where overdense filaments form hydrodynamically and lead to conditions necessary from the Toomre parameter to be less than unity [14]. We now turn to the other, widely accepted model of planetary growth, the *core accretion* model.

2.3.2 Core Accretion

The model of core accretion offers a more gradual and iterative description of giant planet formation as opposed to the sudden collapse in the disk instability model. This model postulates the structure of giant planets as consisting of a solid core and surrounded by an envelope of gas [23]. Such concepts as envelope enrichment or a fuzzy core may be considered in more complicated models of giant planets, although the most basic model is of hydrogen and helium gas surrounding a solid core. There are different phases of growth in the core accretion model, as shown in figure 7. The first phase is the *initial core formation* and results in a solid core with a tenuous or negligible gaseous atmosphere. Much in the same way that terrestrial planets grow, an initial solid core is formed by solid accretion methods, initially brought about by settling and coagulation and further developed by planetesimal or pebble accretion. As the core grows, we reach the second growth phase of *hydrostatic growth*. In this phase, the solid core eventually becomes big enough to gravitationally attract a significant gaseous atmosphere around it. Both solid and gaseous material continue to be accreted, while the gaseous atmosphere remains in hydrostatic equilibrium. As the total mass of the planet, which is the sum of solid and gaseous material, increases, it attracts both more solid and gaseous material, which further strengthens the accretion process and accelerates growth. This process continues to the *crossover mass*, which is the point of mass equality between gaseous and solid material, where gas accretion accelerates significantly and we reach the third phase, the *runaway growth* phase. In this phase, the growth rate is not limited by the physical radius of the planet, rather by the availability of gaseous and solid material in the vicinity around the planet. The growth of the planet is then only terminated by events such as an opening in the gas disk or the dispersal of the gas disk. An illustration of the growth of the core, envelope and total mass is shown in figure 8, detailing the initial rapid accumulation of solids by solid accretion methods, followed by a longer period of hydrostatic growth and then transitioning to runaway growth around the crossover mass.

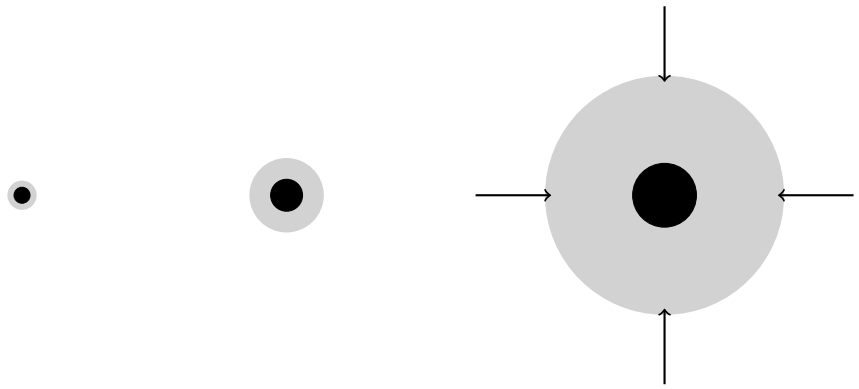

Figure 7: The different stages of the core accretion model. On the left hand side, an initial core is formed quickly with a tenuous atmosphere, then the envelope grows in hydrostatic equilibrium in the middle panel as the core mass becomes large enough. Eventually, on the right hand side, the core mass becomes large enough such that the envelope cannot grow in hydrostatic equilibrium and proceeds to a rapid, runaway growth.

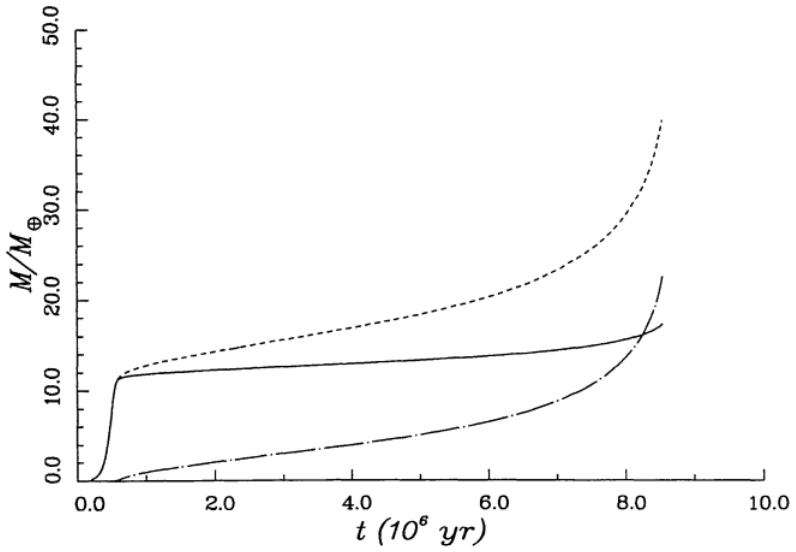

Figure 8: An illustration of the mass growth of a gas giant using the core accretion model. Adapted from Lissauer (1993) [6] using the model from Pollack (1993) [24].

There are two main aspects which led to the general acceptance of the core accretion model [6]. The first is the observation that the core masses of the solar system's gas giant and ice giant planets are of a similar value, and the second is that there exists a critical core mass below which the gaseous envelope grows in hydrostatic equilibrium around the core and above which the gaseous envelope cannot remain in hydrostatic equilibrium and thus collapses [25]. The similar core mass values indicate a common and regulated process which leads to the formation of the gas giant and ice giant planets, since similar core masses through disk instability would be difficult to achieve. As long as the solid accretion rates and the grain opacity of the envelope do not change much over orbital distance away from the host star, the critical core mass value is independent over orbital separation. The critical core mass also allows the gaseous envelope to grow very quickly in mass following collapse by allowing runaway growth as the gas from the solar nebula "falls" into the planet, providing a pathway for the formation of massive gas giant planets. We do not see any significant envelope for the terrestrial planets of the solar system since they did not reach this critical core mass value during their growth, meaning that the primordial envelope attained was eventually dissipated away and the secondary atmospheres of today come from outgassing events.

There do, however, exist issues with the theory. The formation of gas giant planets through core accretion depends strongly on the efficiency of solid accretion. Fragmentation of planetesimals, the planetesimal meter-sized-barrier or early depletion of the feeding zone around the planetary embryo can lengthen growth timescales to the point where the protoplanetary disk dissipates before the embryo can form a gas giant. Some of these issues can be alleviated with pebble accretion, although reaching the necessary core mass of about 10 Earth masses to trigger runaway growth remains a lingering issue with solutions dependent on the system setup. The core accretion model also has difficult predicting the variety of extrasolar systems

we see, with hot-Jupiters and the bimodal distribution of the radius valley requiring further theory to be explained, namely planetary migration and photoevaporation or core-powered loss of the envelope. To understand better the growth of gas giants in the core accretion model, we must better understand the gas accretion process.

2.4 Gaseous Envelope Models

Gas accretion refers to the process of a massive body attracting gas, mainly hydrogen and helium, from the protoplanetary disk. This accretion occurs predominantly through gravitational effects, although there are many other physical factors which influence the rate at which gas is accreted onto the massive body. Since the molecular weight of gas is very low, a sufficiently massive body is required to exert a gravitational force strong enough in order to attract the gas. This means that gas accretion rates are negligibly small for less massive objects, up to the mass of 0.1 Earth masses. Once this rough threshold is passed, however, gas accretion rates become higher and the gas collected onto the planet begins to constitute a non-negligible proportion of the total mass. Gas accretion is an important source of mass addition to a growing planet, since the dominant mass fraction of the gas giant planets in the solar system is hydrogen and helium. The process of gas accretion for planets is still not fully understood and presents some lingering uncertainties, however the main elements of gaseous envelopes and gas accretion are generally agreed upon and provide the backbone for analysis. Much of the analysis in this section comes from Armitage (2020) [8].

2.4.1 Initial Growth

In the core accretion model, the formation of the initial seed for a gas giant planet follows much the same procedure as the accumulation of solid material in the growth of planetesimals. There exists a combination of different mechanisms through which the masses of solids grow. We can determine the mass needed in order for an initial core in the circumstellar disk to be able to retain *at least some* gas by setting the escape velocity of the core equal to the speed of sound in the disk. We can set the escape velocity as

$$v_{\rm esc} = \sqrt{\frac{2GM_p}{R_s}}, \quad \text{with } R_s = \left(\frac{3}{4\pi}\frac{M_p}{\rho}\right)^{1/3}, \tag{24}$$

and rewrite the speed of sound in the disk as

$$c_s = \left(\frac{H}{a}\right) v_K, \tag{25}$$

in order to arrive at the mass needed for a gaseous tenuous atmosphere, given as

$$M_p > \left(\frac{3}{32\pi}\right)^{1/2} \left(\frac{H}{a}\right)^3 \frac{M_*^{3/2}}{\rho^{1/2} a^{3/2}} \tag{26}$$

with a being the orbital radius. This is a very small mass, usually on the order of 1×10^{-4} Earth masses.

More realistically, we can determine the mass needed for the envelope to constitute a non-negligible fraction of the total mass and to be in hydrostatic equilibrium, transitioning into the next phase of growth. This is accomplished by assuming hydrostatic equilibrium in the atmosphere, assuming an ideal gas for the envelope and assuming the outer boundary condition of the Bondi radius. We start with hydrostatic equilibrium,

$$\frac{dP}{dr} = -g\rho = -\frac{GM_p}{r^2}\rho\,, \tag{27}$$

$$\Rightarrow \frac{d\rho}{dr} = -\frac{GM_p}{c_s^2 r^2}\rho\,, \tag{28}$$

$$\Rightarrow \rho(r) = \rho_0 \exp\left[\frac{GM_p}{c_s^2 r} - \frac{1}{2}\right]\,, \tag{29}$$

where we have integrated the hydrostatic equilibrium equation upon inserting the identity for an ideal gas, $P = \rho c_s^2$, and assumed that the outer boundary condition corresponds to the Bondi radius, $r_{\text{out}} = 2GM_p/c_s^2$, and the density at this boundary is ρ_0.

Assuming that most of the envelope mass is at the surface of the planet, we take the envelope mass as

$$M_{\text{env}} \approx \frac{4}{3}\pi R_s^3 \rho(R_s)\,, \tag{30}$$

and search for the condition where $M_{\text{env}} > \epsilon M_p$, with ϵ indicating some sizeable fraction of the total mass, such as 0.1, meaning that the envelope mass is significant. Finding the density at the surface, R_s, to find the envelope mass and substituting this into our above condition gives

$$M_p > \frac{c_s^2 R_s}{G}\left[\ln\left(\frac{\epsilon M_p}{\frac{4}{3}\pi R_s^3 \rho_0}\right) + \frac{1}{2}\right]\,, \tag{31}$$

which, by noting that $M_p = 4\pi R_s^3 \rho_m/3$, can be further simplified to approximately

$$M_p > \left(\frac{3}{4\pi\rho_m}\right)^{1/2}\left(\frac{c_s^2}{G}\right)^{3/2}\left[\ln\left(\frac{\epsilon\rho_m}{\rho_0}\right)\right]^{3/2}\,, \tag{32}$$

where we have neglected the effects of the 1/2 factor within the natural logarithm. Substituting test values into this expression, a body of $\rho_m = 1\text{g/cm}^3$ at 5 AU with $\rho_0 = 2\times10^{-11}\text{g/cm}^3$ and $c_s = 7 \times 10^4\text{cm s}^{-1}$, we obtain $M_p \approx 0.2 M_\oplus$, meaning that a significant envelope in hydrostatic equilibrium forms at approximately 0.2 Earth masses under these conditions [8]. As we can see from equation (32), the mass at which an envelope in hydrostatic equilibrium can form is strongly dependent on the sound speed, which again is dependent on the disk temperature, which is a function of the orbital radius. Therefore growing planets closer to the star, which experience higher disk temperatures, require a higher core mass in order to start forming a significant envelope.

2.4.2 Hydrostatic Regime

Once the envelope reaches hydrostatic equilibrium and becomes optically thick it can be treated using the equations of stellar structure in spherical symmetry [26],

$$\frac{\partial M_r}{\partial r} = 4\pi r^2 \rho \,, \tag{33}$$

$$\frac{\partial P}{\partial r} = -\frac{G M_r}{r^2}\rho \,, \tag{34}$$

$$\frac{\partial L_r}{\partial r} = 4\pi r^2 \rho \left(\epsilon - P\frac{\partial V}{\partial t} - \frac{\partial E}{\partial t} \right) \,, \tag{35}$$

$$\frac{\partial T}{\partial r} = -\frac{3}{16\sigma}\frac{\kappa\rho}{T^3}\frac{L_r}{4\pi r^2} \,. \tag{36}$$

The first equation describes conservation of mass while the second is the statement of hydrostatic equilibrium. The third equation is the conservation of energy equation, where ϵ is the energy source, $V = 1/\rho$ and E is the internal energy per units mass. The last equation is the diffusion equation of radiative transfer where σ is the Stefan-Boltzmann constant and c is the speed of light. We lastly note that κ is the Roseland mean opacity.

The equations (33) to (36) must also be supplemented with equations for the equation of state, Roseland mean opacity and luminosity, in order to be solved, subject to appropriate boundary conditions.

The opacity and luminosity of the envelope play important roles in its structure and growth. The opacity is a measure of how transparent or opaque the envelope is. The total opacity can be decomposed into molecular and grain opacities,

$$\kappa_{\rm t} = \kappa_{\rm mol} + f_g \kappa_{\rm g} \,, \tag{37}$$

where f_g is a grain depletion factor which measures the effect of grains compared to some reference grain opacity, such as the interstellar grain opacity. In regions where the temperature exceeds 170 Kelvin, ice evaporates and the grain opacity reduces. In regions above 1600 Kelvin, silicates are vaporised and the grain opacity drops to zero. The effect of the opacity is to determine the efficiency at which energy is radiated through the envelope and eventually from the protoplanet's surface. The lower the opacity, the more efficiently heat is radiated through the envelope. Heat in the growing planet is provided by the luminosity induced by the solid accretion onto the planet. In this case, the luminosity can be described by

$$L = \frac{G M_{\rm core} \dot{M}_{\rm core}}{R_s} \,, \tag{38}$$

where we can see that the gravitational potential energy of solids accreting onto the growing planet's core is converted to thermal energy.

The balance between luminosity and opacity is an key one. Importantly, if the envelope is allowed to cool by radiating energy outward, the envelope can contract through the *Kelvin-Helmholtz* mechanism. This releases energy in the process, since the gravitational potential

energy of the envelope itself contracting is converted into thermal energy. The reason for this contraction is for the envelope to remain in hydrostatic equilibrium as it radiates energy away. As heat is radiated away, the internal temperature decreases, thereby decreasing the internal pressure. In order for the envelope to remain in a stable hydrostatic equilibrium condition, the envelope must contract in order to raise the internal density and temperature to restore hydrostatic balance. The process depends on how much heat is transferred to the growing planet and how efficiently it is able to radiate this heat away, highlighting the importance and interrelationship between the luminosity and opacity. Changing these factors changes how the envelope can cool and how quickly it contracts, affecting its evolution.

The outer boundary of the gaseous envelope is determined by the minimum of the Bondi accretion radius and the Hill radius. The Bondi accretion radius is given as

$$R_{\text{acc}} = \frac{GM_p}{c_s^2}\,, \tag{39}$$

where c_s is the sound speed of the gas, and determines the radius at which the growing planet can hold onto gas particles from the disk. On the other hand, the Hill radius is given as

$$R_H = \left(\frac{M_p}{3M_*}\right)^{1/3} a\,, \tag{40}$$

where a is the orbital separation from the host star of mass M_*, and determines the radius at which the growing planet's gravitational influence dominates against that of the host star. In order for gas to remain bound to the planet, the radius must be less than both of these values, meaning that the outer boundary is defined as

$$R_{\text{out}} = \min(R_{\text{acc}}, R_H)\,. \tag{41}$$

In order for the envelope to grow during this stage of growth, the accretion rate is given by the requirement that the planet radius is equal to the outer boundary radius. As the gaseous envelope contracts and the outer boundary increases due to solid accretion, gas is added to the planet to maintain the condition that $R_P = R_{\text{out}}$ [23].

There exists a critical core mass above which the envelope can no longer be in hydrostatic equilibrium, as analysed by Mizuno (1980) [25] and Stevenson (1982) [27]. By analysing the structure equations of the gaseous envelope, namely equations (33) to (36), we find a relationship between the core mass and the total mass of a planet in the regime of hydrostatic growth [27] [8] which can be written as

$$M_{\text{core}} = M_{\text{p}} - \left(\frac{C}{\kappa_R \dot{M}_{\text{core}}}\right)\frac{M_p^4}{M_{\text{core}}^{2/3}}\,, \tag{42}$$

where the value of C sweeps up constants and approximate constants, while the opacity κ_R and solid accretion rate $\dot{M}_{\text{core}}$ still play a role in the calculation. This solution provided by Stevenson (1982) [27] is shown in figure 9 alongside the numerical results from Mizuno (1980) [25]. We see that there exists a maximum, critical value of the core mass value given a total

mass, in the regime of hydrostatic equilibrium. Before this point, if more material is added to the planet, there is a contraction and corresponding increase in pressure at the boundary between the core and envelope to compensate this mass increase. The critical mass defines a point where an increase in pressure is not enough to compensate an increase in mass, approximately at $M_{\text{core}} \approx M_{\text{env}}$, and the envelope ceases to be in hydrostatic equilibrium, collapsing on itself. Mizuno showed that if the solid accretion rate and opacity do not vary too much throughout the solar nebula, the protoplanet mass is approximately constant at collapse, which is again reflected in equation (42). The value of the critical core mass increases with increasing opacity, as well as with increasing solid accretion rate. This critical mass point defines a transition point from hydrostatic growth to runaway growth, where the gas accretion rates of giant planets increase significantly.

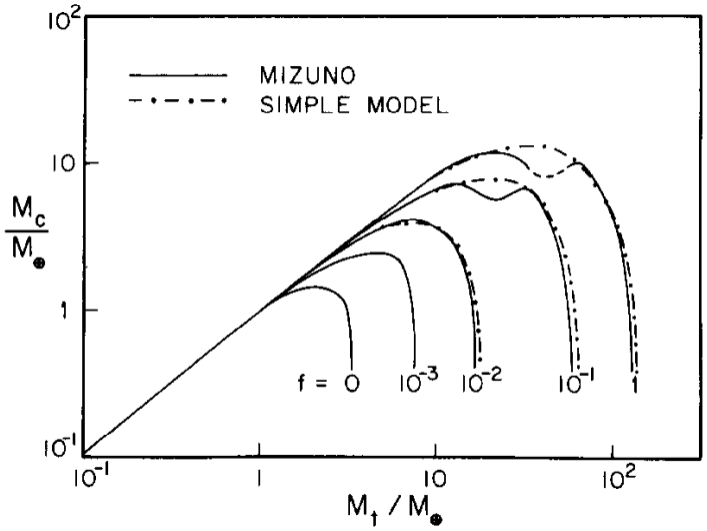

Figure 9: An illustration of the critical core mass from Stevenson (1982) [27]. There exists a maximum, critical value of the core mass, given a system in hydrostatic equilibrium. This critical mass value increases for increasing opacity. The simplified analytical model from Stevenson is plotted alongside Mizuno's computational results.

2.4.3 Gas Accretion Rates

The gas accretion rates used in literature vary considerably, reflecting the high uncertainty of predicting these values. In early work by Pollack et al. (1996) [28], the gas accretion rate is given by the mass of the solar nebula in the shell between the radius of the planet and the outer boundary radius, namely

$$\Delta m_{\text{neb}} = 4\pi R_{bd}^2 \rho_{\text{neb}} \left[R_{bd} - R_p(t + \Delta t) \right] , \tag{43}$$

where the added gaseous mass is determined by the planet radius, R_p, and the outer boundary radius, R_{bd}, either the Bondi accretion radius or the Hill radius. This equation however requires the radius of the planet, a quantity often difficult to obtain. It also does not give an

explicit indication of the gas accretion rate for a given planet mass.

Another approach to determine gas accretion rates is given in Ikoma (2004) [29], in a study investigation the formation of giant planets and the dependencies on solid accretion rates and opacities. The gas accretion rate is estimated as

$$\begin{aligned} \dot{M}_{\text{env}} &= \frac{M_{\text{env}}}{\tau_{\text{grow}}}\,, \\ \tau_{\text{grow}} &= 10^8 \left(\frac{M_{\text{core}}}{M_\oplus}\right)^{-2.5} \left(\frac{\kappa_R}{1\text{cm}^2\text{g}^{-1}}\right) \text{yr}\,. \end{aligned} \tag{44}$$

Ignoring the variation over the opacity, this gas accretion rate is only a function of the core and envelope masses. The advantage of this equation over the gas accretion provided by Pollack et al. (1996) [28] is that the planet radius is not necessary to calculate or include, rather the accretion rate depends only on the mass of the planet, specifically the core and envelope masses. This analytical formulation of the gas accretion rate makes the calculation of the rate very straightforward and applicable to a variety of cases. There is, however, no explicit dependency on the solid accretion rate in this model. Since a more luminous envelope contains more thermal energy, taking longer to cool down, contract and add more gas, and we already know from equation (38) that the luminosity is proportional to the solid accretion rate, the solid accretion rate must pay a role in the gas accretion rate. Equation (44) thus presents itself as an approximate solution to the gas accretion rate.

A more complicated gas accretion rate is offered by Piso and Youdin (2014) [30] and takes into account many influencing factors [31]. The rate is given as

$$\begin{aligned} \dot{M}_{\text{gas}} =& 0.00175 f^{-2} \left(\frac{\kappa_{\text{env}}}{1\text{cm}^2/\text{g}}\right)^{-1} \left(\frac{\rho_c}{5.5\text{g/cm}^3}\right)^{-1/6} \\ &\times \left(\frac{M_c}{M_\oplus}\right)^{11/3} \left(\frac{M_{\text{env}}}{0.1 M_\oplus}\right)^{-1} \left(\frac{T}{81\text{K}}\right)^{-0.5} M_\oplus \text{Myr}^{-1}\,, \end{aligned} \tag{45}$$

where all quantities are self explanatory and f is a "fudge factor" aimed at matching the numerical and analytical results, normally set to 0.2, and results from the fitting procedure over all constituent variables in equation (45).

The above methods for calculating the gas accretion rate represent only a handful of ideas and highlight the variety and uncertainty in calculating gas accretion rates.

2.5 Stellar Classifications

Stars come in a variety of sizes and exhibit changing characteristics during their lifetimes. The characteristics at hand are determined predominantly by the mass of the star. The state of a star can be represented by its luminosity and its temperature, with the Hertzsprung-Russel diagram, hereafter the H-R diagram, detailing the relationship between these two variables

for different types of stars [32]. The H-R diagram shows the temperature as the abscissa, increasing from right to left, and the luminosity as the ordinate, increasing from bottom to top. There exists a main spine of the diagram called the *main sequence*, extending from low temperatures and low luminosities to high temperatures and high luminosities, where the majority of stars live. There exists stellar populations in other regions of the digram around the main sequence, however these characterise other evolutionary epochs of the star, other than the main epoch where the star spends most of its time.

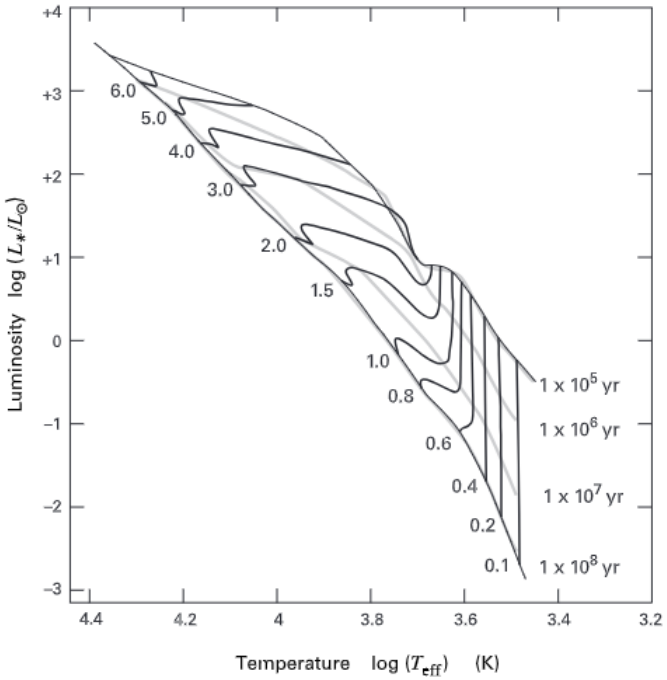

Figure 10: An illustration of the pre-main sequence tracks for stars of different masses. Adapted from Stahler and Palla (2008) [32].

Figure 10 shows the main sequence of the H-R diagram, excluding other stellar populations not on this main sequence. Alongside that, pre-main sequence evolution tracks are shown. These tracks show the evolution of young stars as they contract from their formation to when nuclear fusion of deuterium begins, marking their entry onto the main sequence. These tracks are shown for a variety of stellar masses. Vertical tracks are called *Hayashi tracks* while horizontal ones are called *Henyey tracks*. The vertical tracks indicate that the star is convective, whereas vertical tracks indicate that a radiative zone has developed in the star. From figure 10 we see that low mass stars follow vertical Hayashi tracks until their main sequence entry point. These tracks can be quite long and last a long time, decreasing by many orders of magnitude in luminosity over many tens of millions of years before reaching their main sequence value. This trend continues for higher mass stars, up to about 3 solar masses, where there is a marked decrease in luminosity from formation to entry on the main sequence.

Stars can also be characterised by their spectral type, resulting from measurements of their emission spectra. The emission spectrum of a star is primarily a consequence of the stellar mass, which indicates the values of the temperature and luminosity as shown by the H-R diagram. One classification system in common usage is the *Harvard classification system*, a one-dimensional classification by Annie Jump Cannon [33]. Stars are characterised by their spectral characteristics, reflecting surface temperature, and are assigned a letter according to their type. The classification descends in order of surface temperature as is shown in table 1[3].

Type	Temperature [K]
O	$> 30\,000$
B	$10\,000 - 30\,000$
A	$7500 - 10\,000$
F	$6000 - 7500$
G	$5000 - 6000$
K	$3500 - 5000$
M	< 3500

Table 1: The Harvard stellar classification system. Values taken from LeBlanc (2011) [3].

3 Implementation

The investigation of giant planet formation requires a multitude of models and tools. In order to investigate the effects of orbital radius and stellar mass on the formation of gas giant planets, we simulate the growth of planets up to the crossover mass. The simulations used here consider many physical aspects of the planetary growth process and calculate the amount of gas accreted to the planet iteratively, meaning there is no prescribed function and numerical methods are employed. These simulations are then used fit a variety of fitting functions to predict the gas accretion rates. Finally, we computationally implement these methods, including the fitted gas accretion rates, in order to simulate the growth of gas giants using a fitted gas accretion functions.

3.1 Simulations

In order to obtain detailed data on the growth of planets, we need to accurately simulate the growth of these planets. For this purpose, the software "Modules for Simulations in Stellar Astrophysics", hereafter MESA, is used [34]. More specifically, the version mesa-r24.03.1 is used. The original purpose of MESA is to simulate stellar astrophysics, however, we can adapt this software to simulate planets, since the envelopes of gaseous planets are mathematically treated the same way as stars. This adaptation was performed by Valletta and

Helled (2020) [35] and is used in this investigation in order to investigate gas giant formation.

Figure 11 shows illustratively how gas is accreted to the growing planet during the simulation. The simulation in MESA works in an iterative manner, where all quantities at a given timestep calculated, physical quantities adjusted accordingly, the simulation progressed to the next timestep and the process repeats again. As shown in figure 11, at timestep t, the density profile as a function of radius is given by a constant value up to the core radius, R_{core}, then a decaying function up to an original accretion radius, R_{acc}, smoothly transitioning into the solar nebula density which is locally constant. In the physical calculations during the simulation, the envelope is sectioned into many slices and quantities such as luminosity or density are calculated for each layer and stitched together. Due to Kelvin-Helmholtz contraction, the planetary radius shrinks from the accretion radius to a planet radius R_p. This induces a gap in between the physical planet radius and the radius of accretion. Gas is introduced into this gap from the gravitational attraction of the existing core and envelope mass, as well as solid material accreting onto the core. Although the increased mass increases the radius of accretion, the planetary radius increases enough to equal the eventual accretion radius and we arrive at the new density profile, the profile at $t + \Delta t$. The gas accretion rate is given by the amount of gas added in this iterative process divided by the amount of steps needed to reach it. As seen in the figure, the density profile in the envelope attains a new shape, reflecting the added mass and the increased accretion radius.

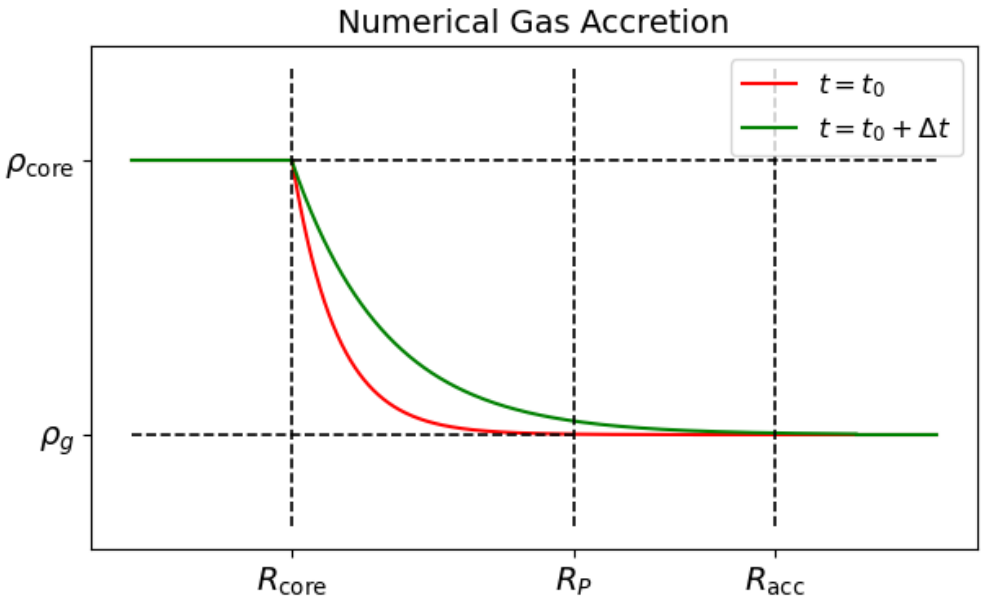

Figure 11: A simplified illustration of the numerical gas accretion scheme used in MESA.

For each simulation, we assume an initial solid core of 0.1 Earth masses and a gaseous envelope of 1×10^{-7} Earth masses. This initial planetary seed is then embedded in the protoplanetary disk for a given stellar mass and orbital radius and the outer boundary conditions matched to the values of the disk model, described within section 2.1. The interior

model of the planet is assumed only to consist of a core of solid material and a gaseous envelope with no enrichment. The accretion of solids means that solids must impact the envelope, which may cause fragmentation leading to solid enrichment of the envelope. This process is, however, not accounted for, and we assume that all solid material sinks to the core. The simulations also assume a fixed orbital radius for the growth of the planet, with no planetary migration considered. In all cases, pebble accretion is the mechanism of solid accretion.

Two stars are investigated, namely a solar mass star, $1M_{\odot}$, and a star of 0.2 solar masses, $0.2M_{\odot}$. The model for the solar mass star is the self similar solution from section 2.1, while the model for the $0.2M_{\odot}$ star will be described shortly in section 3.2. For all cases it is assumed that the metallicity of the disk reflects the solar metallicity, and is taken as $z = 0.01$. The temperature profile for the M-type star of 0.2 solar masses is given in section 3.2, while the temperature profile for the G-type star of solar mass is taken from Chiang and Goldreich (1997) [36], given as

$$T(r) = 150 \left(\frac{r}{1\text{AU}}\right)^{-3/7} . \tag{46}$$

The orbital radii investigated around the solar mass star are at 3, 5, 7, 9 and 11 AU, and are believed to represent a good spread of possible formation locations of a gas giant. The investigated radii around the star of mass $0.2\text{M}_{\odot}$ are 1.75, 2.92, 4.09, 5.26 and 6.43 AU. These correspond to the same dynamical time as the distances for the G-star and have the same corresponding orbital periods.

Evolutionary simulations are also briefly considered during the investigation. In the case of no evolution, we keep the disk model fixed at the value given at time 8×10^5 years. In the evolving case, we allow this value to increase during the simulation and evaluate the disk surface density at the corresponding timestep value. The disk surface density decays over time, leading to lower values of accretion rates than in the non-evolving case. The solid disk density as taken as a metallicity fraction of the gas disk, obtained by multiplying the gas disk surface density by the metallicity, Z.

The outer boundary conditions are also of great importance in the MESA simulations. For each simulation case considered, an initial, preloaded model which is created at 7 AU around a solar mass star needs to be smoothly relaxed to the conditions for the simulation in question. This involves a gradual evolution of the model to match the outer boundary conditions given. If the outer boundary conditions are not correct or accurate, the simulation may not converge and returns an error. The conditions necessary to provide are the temperature and pressure at the outer boundary.

In all investigations, the simulation is terminated when crossover mass is reached or when the time elapse reaches 1×10^8 years. We also take the grain opacity factor to be $f = 1$ in all cases. A full account of the model parameters and outer boundary conditions used in the MESA simulations is available in the Appendix.

Once the gas accretion rates are fitted using the data from the MESA simulations, the rates are implemented into the PYTHON programming language. This is advantageous since

the simulations in MESA are slow and prone to errors, whereas the PYTHON simulations, using the fitted gas accretion rates, are quick and easy to simulate. The simulations work by initially defining the solid mass and the envelope mass, the calculating the pebble solid accretion rate and the gas accretion rate from a given fitting function of choice. These new values are added to the array of masses and the process continued iteratively. The simulation is terminated either when the crossover mass is reached or when the total simulation time reaches 1×10^8 years. The timestep interval is chosen as ten years, which is deemed accurate enough to capture the fine resolution of the planetary growth. In order to simulate planets orbiting stars which are neither 1 not 0.2 solar masses, we need to define a transitionary mass past which we stop using the M-disk model as defined in section 3.2 and return to using the gas disk model for the G-star. We define this mass to be 0.6 solar masses. Planets forming below this mass use the M-star disk model, while planets orbiting stars of mass greater than or equal to this use the previously defined G-star disk.

3.2 M-star Disk Models

Disk properties vary with the stellar classification of the host star, which suggests that the planetary formation process differs over stellar mass [37] [38]. In this motivation, we highlight another disk model appropriate for use around M-stars, from Zawadzki, Carrera and Ford (2021) [38]. The gas surface density is obtained from the equation

$$\dot{M} = 3\pi\nu\Sigma\,, \quad \Rightarrow \Sigma = \frac{\dot{M}}{3\pi\nu}\,, \tag{47}$$

where the mass accretion rate, $\dot{M}$, is proportional to the disk viscosity, ν, and the gas surface density, Σ.

The viscosity is taken from the α-disk model as

$$\nu = \alpha H c_s\,, \tag{48}$$

where the disk scale height and sound speed in the disk are given, respectively, as

$$H = \frac{c_s}{\Omega}\,, \quad c_s^2 = \frac{k_B T}{\mu m_H}\,, \tag{49}$$

for a Keplerian orbital frequency Ω. The temperature profile is given by the composition of two separate profiles representing two separate heating regimes. The main heating regime in the inner disk is dominated by viscous heating while the outer region is dominated by irradiation from the host star. For an α value of 10^{-3}, the viscous heating profile is given as

$$T_{\text{visc}} \simeq 123.4 \left(\frac{\dot{M}_*}{10^{-8}\text{M}_\odot\text{yr}^{-1}}\right)^{2/5} \left(\frac{r}{1\text{AU}}\right)^{-3/7} \text{K}\,, \tag{50}$$

and the irradiative temperature profile, which depends on the host star luminosity, given as

$$T_{\text{irr}} \simeq 188.8 \left(\frac{L}{1\text{L}_\odot}\right)^{2/7} \left(\frac{r}{1\text{AU}}\right)^{-3/7} \text{K}\,, \tag{51}$$

with the effective temperature profile given by

$$T(r) = \left(T_{\text{visc}}(r)^n + T_{\text{irr}}(r)^n\right)^{1/n} , \tag{52}$$

where $n = 20$, and the luminosity of a 1 million year old star of $0.2M_\odot$ with $Z = 0.01$ is $0.26L_\odot$.

The other parameter of equation (47) in the determination of the gas surface density is the accretion rate $\dot{M}$. This is given as

$$\dot{M} = \left(1.8 \times 10^{-8}\right) \left(\frac{\dot{M}_*}{0.7\text{M}_\odot}\right)^2 \left(\frac{t}{1\text{Myr}}\right)^{-1} \text{M}_\odot\text{yr}^{-1} . \tag{53}$$

3.3 Savitzky-Golay Filters

The gas accretion rate from the MESA simulations returns a very noisy signal and oscillates strongly. This noise introduces complications into the fitting of functions and raises questions on the accuracy of the fit. We therefore need a method of smoothing the data to mitigate the effects of the noise. We choose to use Savitzky-Golay filtering, which is a method of smoothing digital signals of discrete points [39]. These are commonly used in signal processing applications where a signal may be influenced by noise-inducing factors, leading to a collection of points which require smoothing in order to extract the meaningful signal. Care must be chosen when smoothing a signal, since the pursuit of eliminating noise can result in the elimination of important characteristics about the signal. We choose to apply this particular filter to our gas accretion rate signal since it is a method of smoothing the data while also retaining feature and quirks about the signal itself.

The *Savitzky-Golay* filter works by taking a range of points around a given point, x_k, then fitting a polynomial to these points. The smoothed value given by the evaluation of the polynomial at the corresponding point x_k. Specifically, we take a polynomial of the form

$$y = \sum_{i=0}^{p} a_i x^i , \tag{54}$$

and determine the coefficients by the linear least squares fit

$$\sum_{i=-m}^{m} \left(y_{k+i} - \sum_{j=0}^{p} a_j x_{k+i}^j\right)^2 . \tag{55}$$

The filtering process depends on two parameters, namely the *window length*, $2m + 1$, and the *polynomial order*, p. The window length determines the number of points used in each polynomial fit, with point x_k being the center of the window, while the polynomial order is self explanatory. Note that the window length must be an odd integer, since we need an equal range on both sides of the point x_k, leading to $2m + 1$ values. The window length must also be larger than the polynomial order, $2m+1 > p$ in order for unique polynomial determination.

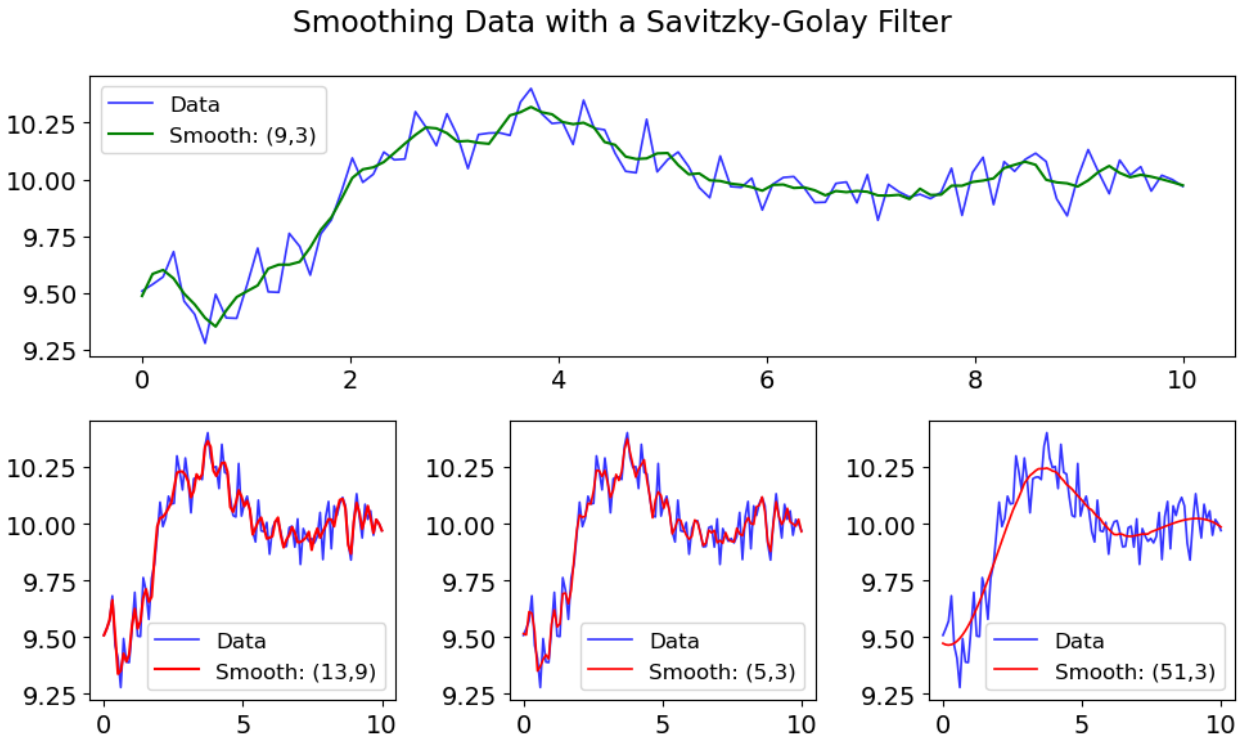

Figure 12: A toy example implementation of a Sovitzky-Golay filter. Different window lengths and polynomial orders are used to smoothen an exponentially decaying sinusoid. A correct choice of window length and polynomial order is not strictly defined and good values depend on the dataset in question.

In figure 12 we see the Savitzky-Golay filter applied to a noisy, decaying sinusoid function. The quality of the smoothing depends on the choice of the window length and the polynomial order. Too wide a window length averages the data too much, losing detail, whereas too narrow a window length matches the data too closely, losing the ability to perform smoothing. Similar effects hold for the polynomial order. There is no correct choice for the window length and polynomial order, rather the choice depends on the problem and the data in question.

4 Investigation and Results

4.1 Initial Observations

The first results from the MESA simulations are shown in figures 13 and 14, where the gas accretion rate as a function of relevant parameters is plotted. The simulations were stopped when the crossover mass was reached, meaning that the envelope mass equals the core mass. This crossover mass becomes lower as the orbital radius away from the host star is increased, as well as when the host star mass is decreased. This points to the first observation we make, that the total mass at crossover is not constant and only dependent on the disk parameters, rather it depends on the system parameters. We also note that the timescales involved to

reach crossover mass for the G-type star are within the estimations of the disk lifetime, while the timescales around an M-type star teeter on the edge or lie outside the disk lifetime estimations. We conclude that, based solely on the time to crossover mass and with estimations of disk dispersal times, it is less likely that a growing planet around an M-type star will form before the dispersal of the disk.

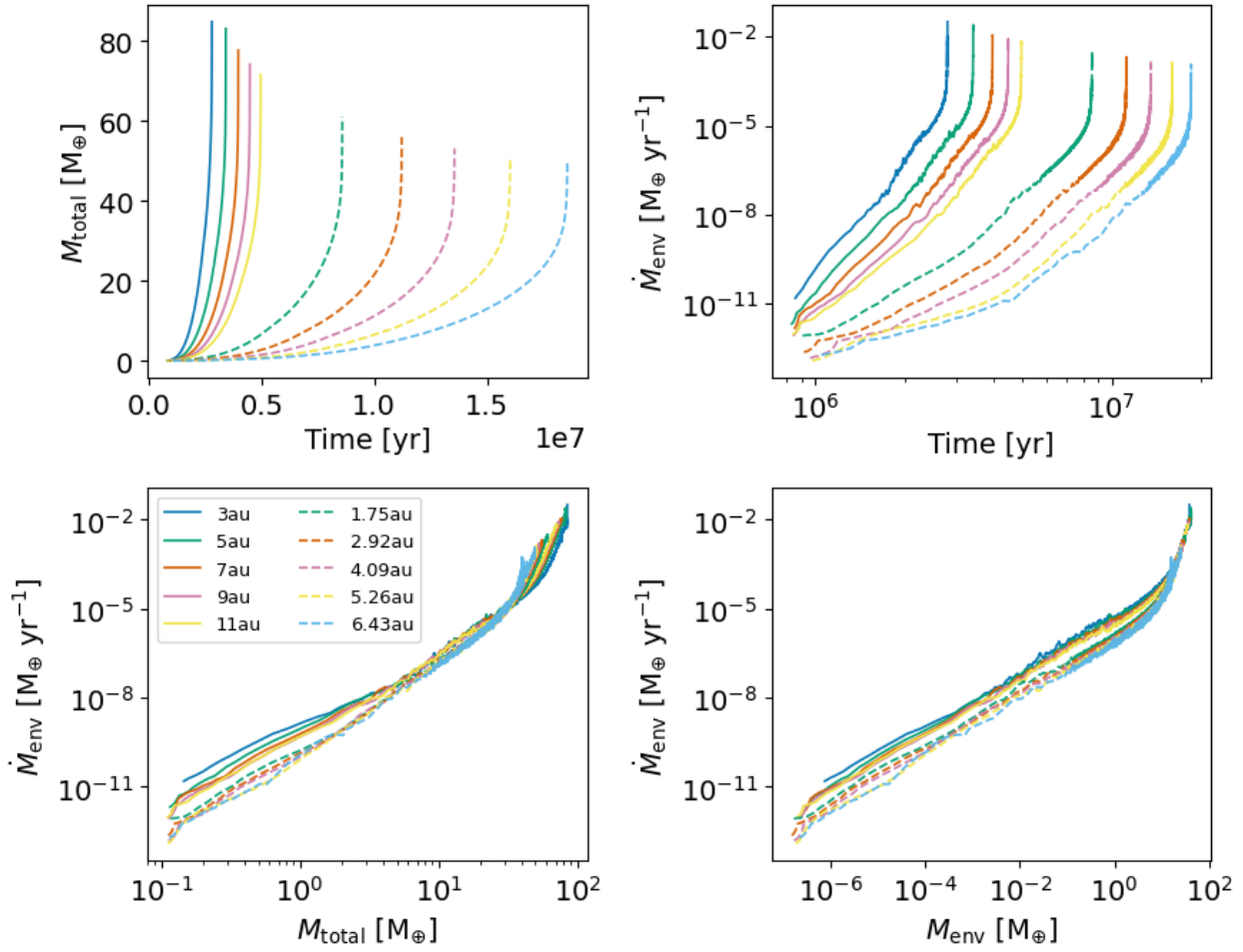

Figure 13: Gas accretion rates over relevant variables for relevant cases for the MESA simulations. We note that the orbital radii values implicitly indicate the stellar type involved, since unique orbital radii are investigated for the solar mass star and the $0.2M_\odot$ star. The solid lines correspond to the G-star and the dashed lines to the M-star. These panels only include the cases with non-evolving disks.

The higher total mass at crossover for planets closer to the host star and around heavier stars follows primarily from a difference in the solid accretion rates. If the solid accretion rate is higher, more solid mass will be accreted quicker, meaning that more gaseous material needs to be added in order to reach equality at the crossover mass. We can see from figure 13 that the gas accretion rate is a strong function of the total mass of the planet. In order for the gas accretion rate to outpace a high solid accretion rate and reach the crossover mass, the

planet needs to be massive enough such that the gas accretion rate will become high enough to add enough material to reach the crossover mass. So given a higher solid accretion rate, a higher total mass is needed to accrete gaseous material at a high enough rate in order to overtake the high solid mass already accrued. Since a high accretion rate naturally leads to a higher total mass quicker, leading to a more rapid onset of strong gas accretion, this process happens naturally, resulting only in a shortened time needed to crossover mass and a higher total mass at crossover.

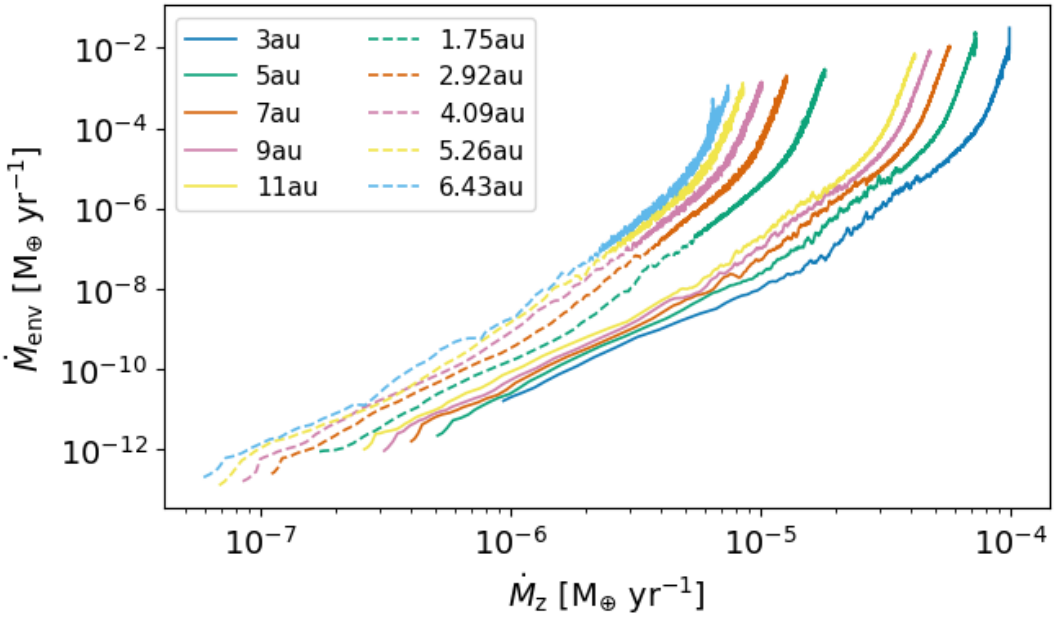

Figure 14: The gas accretion rate as a function of the solid accretion rate. The gas accretion rate for a given solid accretion rate is higher for a planet further away from the host star and around a lower mass star. The solid lines correspond to the G-star and the dashed lines to the M-star.

We also see that the gas accretion rate increases monotonically over time and is higher at any given time for a growing planet closer to the star and around a higher mass star. The behaviour of the gas accretion rate over time strongly resembles the plot of the total mass over time, given that the gas accretion rate strongly depends on the total planet mass. This can be seen in figure 13 where the gas accretion rates over all cases are similar for a given planet mass although, very importantly, not the same. There exists a difference due primarily to the difference in solid accretion rates for the different cases. This can be seen in figure 14, where the gas accretion rates are plotted as functions of the corresponding solid accretion rates. The first observation we can make here is that, for a given solid accretion rate, the gas accretion rate is different for the different cases. Interestingly, the order of the cases, which we see as the colouring of the lines, reverses when we compare it to the plot of the gas accretion rates over time. Even though the gas accretion rate at a given time is smaller for a planet far around an M-star, the gas accretion rate *for a given solid accretion rate* is highest in this case. We can link the total planet mass and the solid accretion rate in

order to provide an interpretation for this observation. From figure 6 we know that the solid accretion rate increases for higher mass stars, for higher mass planets and for orbits closer to the host star. This is reflected in the initial solid accretion rates in figure 14 where the initial solid accretion rates are higher for the 3 AU G-star case and lowest for the 6.43 AU M-star case, even though the initial mass of the planetary embryo is 0.1 Earth masses in all cases. The higher solid accretion rate of a planet close to a massive star for the same mass means that a growing planet far away from an M-star needs a much higher mass in order to have the same solid accretion rate as the lower mass growing planet close to a G-star. From figure 13, however, we see that the gas accretion rate is a strong function of the planet mass. This means that even though a more massive growing planet far from an M-star has the same solid accretion rate as a lower mass body close to a G-star, the gas accretion rate is higher because the mass of the planet is higher. Therefore, for a given, equal solid accretion rate, the mass of a planet further away and around a lower mass star must be higher and therefore the gas accretion rate is higher, since it is mainly a function of the planet mass. The gas accretion rate is mainly a function of the planet mass since the rate at which gas accretes to the planet is a reflection of how well the gravitational pull of the planet is able to scrape away gas from the surrounding solar nebula, and more gas is scraped away for a stronger gravitational pull from a more massive planet. This interpretation explains our observations in figure 14, since we now understand that, for a given solid accretion rate, the gas accretion rate for a planet with a larger orbital separation and around a lower mass star is higher since the total mass of the planet is higher at this solid accretion rate, meaning a higher gas accretion rate. This also hints at the effects on metallicity. For the same mass, the solid accretion rate far around a low mass star is lower than a planet close around a massive star, however the gas accretion rates are similar, given the strong dependence on total mass. Therefore, in the former case, more gas is being added as compared to solids, logically leading to a lower planet metallicity.

These observations show a very important result about the gas accretion process, namely that the strength of the gas accretion rate changes over orbital radius and stellar mass. These factors need to be taken into account when estimating the gas accretion rate.

4.1.1 Evolving Disks

In reality, circumstellar disks evolve and exhibit a declining column density over time. This affects the growth of planets leading to reduced rates of growth, since the availability of solid material declines over time, leading to reduced accretion rates. Figure 15 shows the total mass over time for the non-evolving disk cases in colour and the evolving disk cases in black. We note that the timescales for growth are lengthened considerably. The timescale for a planet around a G-star at 5 AU in the non-evolving case is approximately 3 million years, whereas it extends to approximately 6 million years in the evolving disk case. This represents almost a doubling in the timescale involved and is the difference between a gas giant planet forming and not forming, considering disk dispersal. The second thing we note is that the total mass at crossover is lower for the evolving disk cases than for the non-evolving disk cases. Given the reducing solid accretion rates around the growing planet due to disk evolution, the planet grows at a slower rate meaning that the mass of the planet at a given time

is lower than otherwise. Also, since the solid accretion rates would be lower with evolving disks, the analysis by Mizuno (1980) [25] shows us that the critical core mass needed for the collapse of the envelope out of hydrostatic equilibrium would decrease as well at this point. This means that runaway gas accretion can occur at an earlier core mass value, leading to a lower total mass at crossover. We also realise that, since the mass of the core would be lower at the onset of runaway growth and combining with the lower solid accretion rates, the metallicity of a planet at disk dispersal would be lower in the evolving disk case than in the non-evolving case. This highlights the importance of disk evolution and of solid accretion rates in the determination of a gas giant planet's properties.

The third thing we note is that the evolving disk cases around an M-type star never actually reach the crossover mass. From figure 16 we see a sharp qualitative difference between the behaviour for evolving disks around M-type stars and the behaviour of the other cases. The solid accretion rates for these cases, highlighted in red in the figure, actually *decrease* over time, from their starting initial values. The gas accretion rates on the other hand are always monotonically increasing. The reason for the decreasing solid accretion rates is that the availability of solid material in the disk decreases faster than the rate at which the planetary embryo can grow, increase its Hill radius and compensate for the disk evolution. Although the solid accretion rates are still positive, leading to a net growth in mass over time, the rate decreases, leading to a failed gas giant planet. This behaviour does not depend on any reasonable disk dispersal time and the success of a planet growing to a gas giant is only dependent on the rate of disk evolution compared to the solid accretion rate.

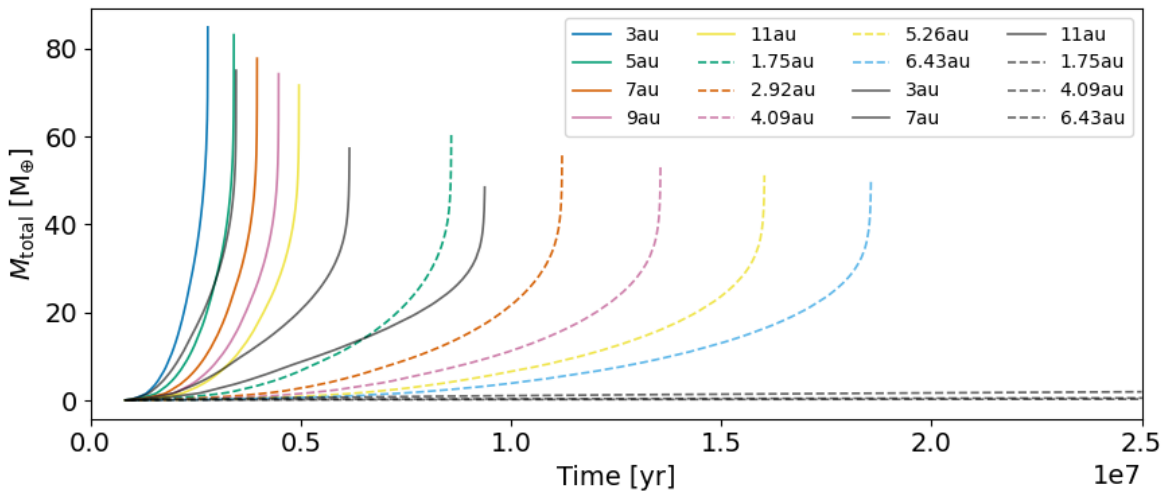

Figure 15: The total mass over time for both non-evolving and evolving disks.

In a similar vein, we see that the solid accretion rates for the evolving cases around a G-type star, highlighted in black in the figure, are not as high as their non-evolving counterparts, although they do increase monotonically. Since the solid accretion rates increase over time, we achieve the crossover mass and a gas giant planet. If the disk evolution in these G-type star cases were quicker, we may reach a case where the solid accretion rates are not large

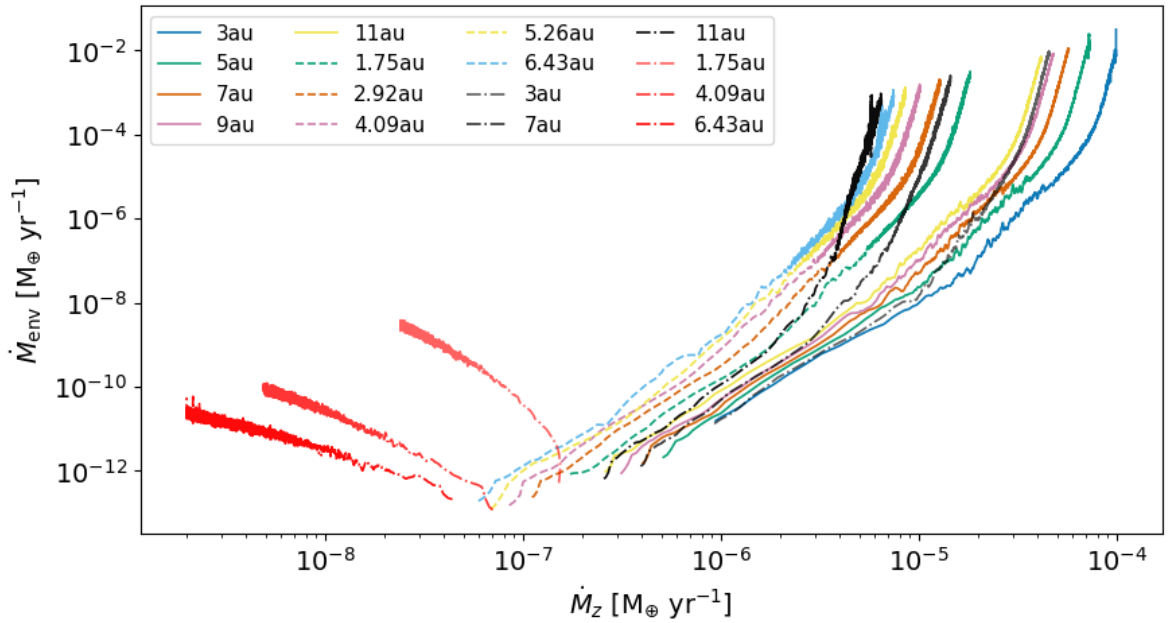

Figure 16: The gas accretion rate as a function of the solid accretion rate for non-evolving and evolving disks.

enough to compensate for disk evolution and the trajectory of the G-star lines would "tip over" and the solid accretion rates would decrease monotonically, joining their M-star counterparts. The balance between the rate of disk depletion and solid accretion is an important one, dictating the success or failure of a gas giant planet.

4.2 Fitting the Gas Accretion Rates

To understand better the gas accretion process and to be able to calculate gas accretion rates, we proceed to fit a function to the simulation data. This is necessarily a data driven approach since analytically derived models of gas accretion rates are, although highly sought after, difficult to derive and are not the goal of this thesis. The aim of this section is to find a robust method to calculate gas accretion rates and through this, to gain further insight into the gas accretion process for the different cases investigated.

We will start by implementing and analysing the performance of previous work. Then we will attempt to implement new concepts for fitting functions in increasing order of complexity. The performance will be assessed and a conclusion drawn on the most effective method to model the gas accretion rates.

Before we begin fitting different functions to predict the gas accretion rates, we need a method of quantitatively assessing the fit to the data. We choose to define a weighted root mean

squared function, WRMS, to evaluate fitting quality, given as

$$\text{WRMS} = \sqrt{\frac{\sum_i^n (y_i)(y_i - y_{*,i})^2}{\sum_i^n y_i}}, \tag{56}$$

where y_i are the calculated points and $y_{*,i}$ are the data points from the MESA simulations. We linearly increase the weight according to the gas accretion rate, since higher gas accretion rates are more important as they contribute more mass to the planet in a given time period. The scaling of the weighting is arbitrarily chosen as being linear. We **importantly** note that the weighted root mean squared calculation is always performed in $\log_{10}$ space, meaning that the base ten logarithm of the calculated and simulated data points, y_i and $y_{i,*}$, are used in equation (56).

4.2.1 A Previous Fit

Immediately skipping over the more basic models to calculate gas accretion rates, we investigate a previous fit by Eriksson et al. (2023) [40] which models the gas accretion rate as

$$\dot{M}_{\text{gas}} = \dot{M}_{\text{gas},1} + \dot{M}_{\text{gas},2}, \tag{57}$$

where

$$\dot{M}_{\text{gas},1} = 10^{a_1} \left(\frac{M_{\text{core}}}{1\text{M}_\oplus}\right)^{b_1} \left(\frac{\dot{M}_{\text{solid}}}{10^{-7}\text{M}_\oplus/\text{yr}}\right)^{c_1} \text{M}_\oplus/\text{yr} \tag{58}$$

$$\dot{M}_{\text{gas},2} = 10^{a_2} \left(\frac{M_{\text{core}}}{1\text{M}_\oplus}\right)^{b_2} \left(\frac{M_{\text{env}}}{1\text{M}_\oplus}\right)^{c_2} \left(\frac{\dot{M}_{\text{solid}}}{10^{-7}\text{M}_\oplus/\text{yr}}\right)^{d_2} \text{M}_\oplus/\text{yr} \tag{59}$$

and with parameters for the two grain opacities, $f_g = 0.1$ and 1.0 given in table 2. For the work presented here, we choose the parameters corresponding to a grain opacity factor of 1.

	$f_g = 1.0$	$f_g = 0.1$
a_1	-8.655389	-8.058656
b_1	3.488167	3.262527
c_1	-0.449784	-0.464667
a_2	-10.725292	-11.188670
b_2	3.989025	5.834267
c_2	2.415257	2.880980
d_2	-0.307779	-1.116815

Table 2: Parameters in the gas accretion fit from Eriksson et al. (2023) [40].

The above equation (57) consists of two separate regimes, a first regime where the gas accretion rate is dictated by the core mass and the solid accretion rate, with a second regime where

the envelope mass is included. The second regime, given by the second term of equation (57) only becomes relevant once there is a significant envelope mass and then comes to dominate over the first term, given the significant exponent of c_2 in table 2.

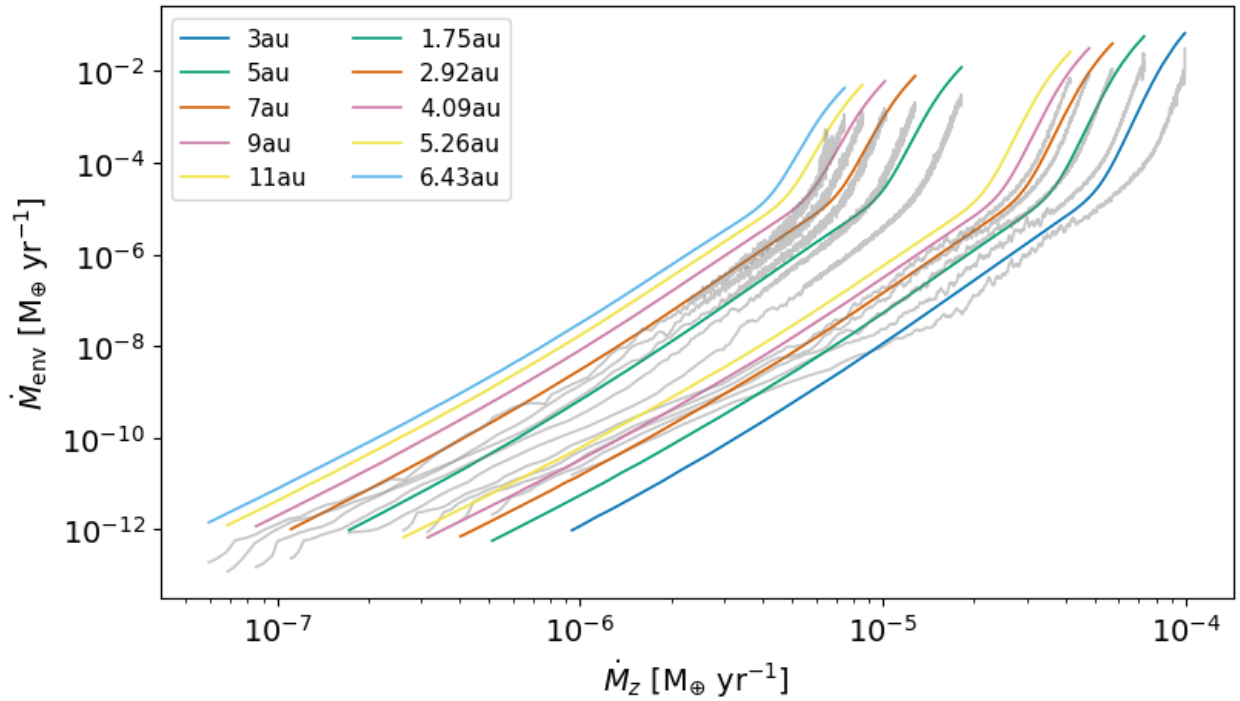

Figure 17: The gas accretion rate predictions with simulation data overlayed. Predictions are taken from the model of Eriksson et al. (2023) [40] and we choose the solid accretion rate as the independent variable.

We can assess the performance of the fit by applying the function to the simulation data. This fit using the prescribed formula from equation (57) and the parameter follows corresponding to a grain factor of 1, we find the results in figure 17. Although the fitting function is a function of three separate physical parameters, we choose to plot over the solid accretion rate for visual presentation.

Upon visual inspection, we see that the fit tracks the general behaviour of the simulation data, however fails to provide the actual values. The predicted values consistently overestimate the gas accretion rates, meaning that the timescales calculated for planetary formation are shorter than those from the simulation. A fit for the exponents in equation (57) in log space reduces to a least squares minimisation over each constituent variable, or in other words, a straight line is fitted over the data for that variable. Given the natural upturn in the gas accretion rates at the end of the simulation data for each of the core mass, envelope mass and solid accretion rate, as in figure 13, fitting a straight line is certain to overestimate the data, since the upturn at the end will shift the slope of the fitted line upwards. The weighted root mean square values for this fit are shown in table 3 .

Star Mass [$M_\odot$]	Orbital Radius [AU]	WRMS	Avg. WRMS	Total Avg. WRMS
1	3	0.9040	0.833	0.957
1	5	0.8193		
1	7	0.8071		
1	9	0.8124		
1	11	0.8224		
0.2	1.75	1.0477	1.081	
0.2	2.92	1.0580		
0.2	4.09	1.0817		
0.2	5.26	1.1056		
0.2	6.43	1.1122		

Table 3: The Weighted root mean square values for the fitting function from Eriksson et al. (2023) [40].

Also, around a gas accretion rate of approximately 10^{-5} Earth masses per year, we see in figure 17 that there is a significant increase in the gas accretion rate, however the curvature of the simulation data and prediction in this regime are different. In the simulation data, the gas accretion rate growth is always accelerating, however in the predicted fit, the growth accelerates sharply and then decelerates. As well as overestimating the growth rate, this changes the growth trajectory of the forming planet over time, leading to inaccurate estimations of the mass and other physical parameters during the evolution of the growth.

If we are very intent on performing a correction to equation (57) to account for the orbital radius and the stellar mass, we can include radial and stellar mass correction factors to the equation and fit the exponents using the data. We define a corrective fitting function as

$$\log_{10}(\dot{M}_{\text{env}}) = \log_{10}(\dot{M}_{\text{env, 7 AU, 1 M}_\odot}) + \alpha \log_{10}\left(\frac{r}{7\text{AU}}\right) + \beta \log_{10}\left(\frac{M_*}{1M_\odot}\right), \tag{60}$$

where we see that the fit at 7 AU around a solar mass star is shifted depending on the orbital separation and stellar mass. The result of this procedure is illustrated in figure 18, where we have obtained the result

$$\alpha = -0.6376\,, \qquad \beta = 1.1968\,. \tag{61}$$

By visual inspection we see that the corrective fits in colour track the original fits shown in black, meaning that the corrective fit performs approximately the same as the original fit, with weighted root mean squared values given in table 3. This arises from the original error given in the fit at 7 AU around a solar mass star. Performing a corrective fit to shift the result over orbital radius and stellar mass still propagates the original error induced by an inaccurate fit.

The aforementioned issues regarding consistent overestimation of the gas accretion rates contribute in leading to inaccurate estimations of the planetary growth, necessitating the

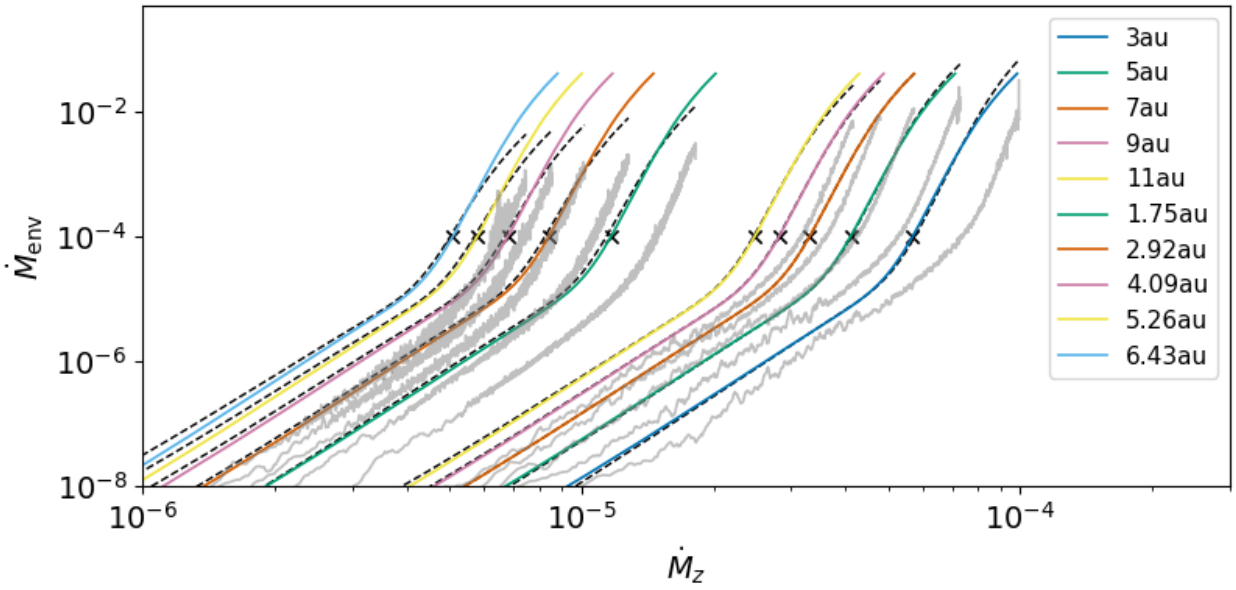

Figure 18: Correcting the fit by Eriksson et al. (2023) [40] using radial and stellar mass correction factors. The gas accretion fit applied individually to each dataset is shown in dashed black, while the corrective fit using the orbital separation and stellar mass is shown in colour. The inherent error induced by the fitting function remains even after correction.

development of a different gas accretion equation. To this we now turn our attention.

4.2.2 Polynomial Fitting

A natural and straightforward method of performing a fitting function is to fit a polynomial to an appropriate variable. In this way, the gas accretion rate can be calculated simply as a function of one variable, which makes a fit very tractable and straightforward to implement. The difficulty is to find an appropriate variable over which to perform the fit. A variable needs to exhibit the right behaviour to be fitted with a polynomial, and that this behaviour is consistent across the different cases in order for the method to remain robust. We can begin by choosing some relevant variables over which to fit a polynomial. In figure 19 we explore the suitability of a variety of variables for polynomial fitting. For each variable and in each case, the third order polynomial of best fit is shown alongside the simulation data, with the averaged weighted root mean square given in table 4. Note that only cases with a non-evolving gas disk are included here. A third order polynomial is chosen in each case since it is expected to capture the complex behaviour of the gas accretion rates without overfitting to the data. For each considered variable, we fit the polynomial

$$\log_{10}(\dot{M}_{\rm env}) = ax^3 + bx^2 + cx + d\,, \tag{62}$$

to the data in $\log_{10}$ space, where x is the base 10 logarithm of the independent variable we consider. The solutions are translated back out of $\log_{10}$ space in figure 19, however with

logarithmic scaling on the axes.

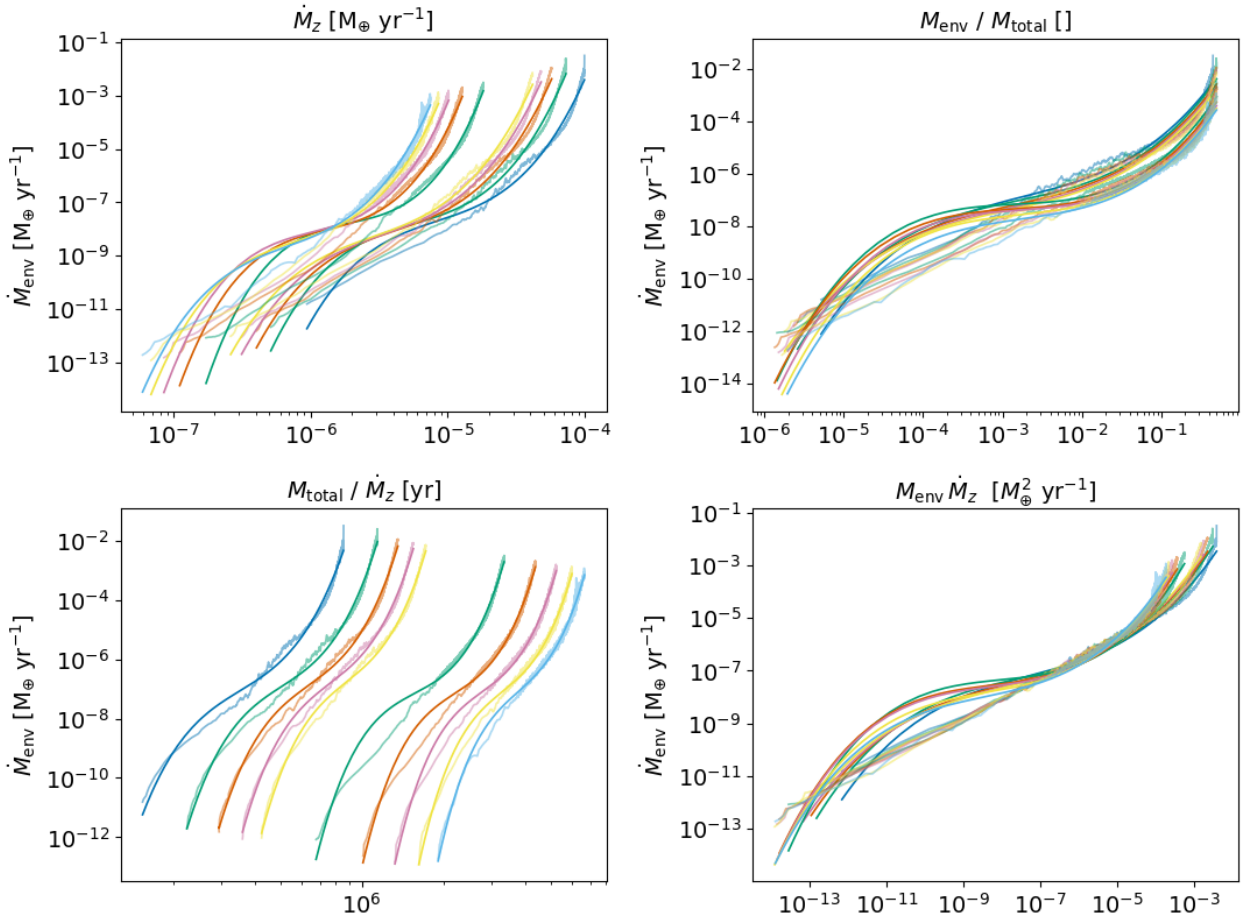

Figure 19: Exploring the potential of fitting a polynomial to a variety of test variables in order to predict the gas accretion rates.

Variable	Avg. WRMS
$\dot{M}_z$	0.2094
$M_{\rm env}/M_{\rm total}$	0.2640
$M_{\rm total}/\dot{M}_z$	0.1465
$M_{\rm env}\,\dot{M}_z$	0.2375

Table 4: The averaged WRMS values for a polynomial fit of the gas accretion rate over the named variable. The total mass divided by the solid accretion rate distinguishes itself as the most suitable candidate for polynomial fitting.

We conclude that the total mass divided by the solid accretion rate is the most appropriate variable to use for polynomial fitting, given the low average of the weighted root mean

squared values and the distinct separations between the cases for the different orbital radii and stellar type. We proceed in this section by implementing polynomial fits with this chosen variable.

As shown in figure 20, we can plot the best fit polynomial for each case, including both non-evolving and evolving gas disks, and show the coefficients of best fit. We note that the behaviour of the evolving disk cases is quite different to that of the non-evolving cases, with the growth tracks for the evolving M-stars looking more like linear fits than polynomial fits. The prediction of the coefficients of best fit also seems non-trivial to perform. If we take, for example, the first coefficient, a, on the left hand side of figure 20, we see that the coefficients for G-type stars in the non-evolving case are more constant than for corresponding M-type stars, and that the curvature in the trend over orbital separation is upwards rather than downwards as for M-type stars. When we then include the evolving cases, we see a large change in magnitude and a difference in the trend over orbital separation. It is difficult to interpolate between the behaviours of the points for each stellar mass and to make inferences on the change in behaviour over orbital radius for each stellar type.

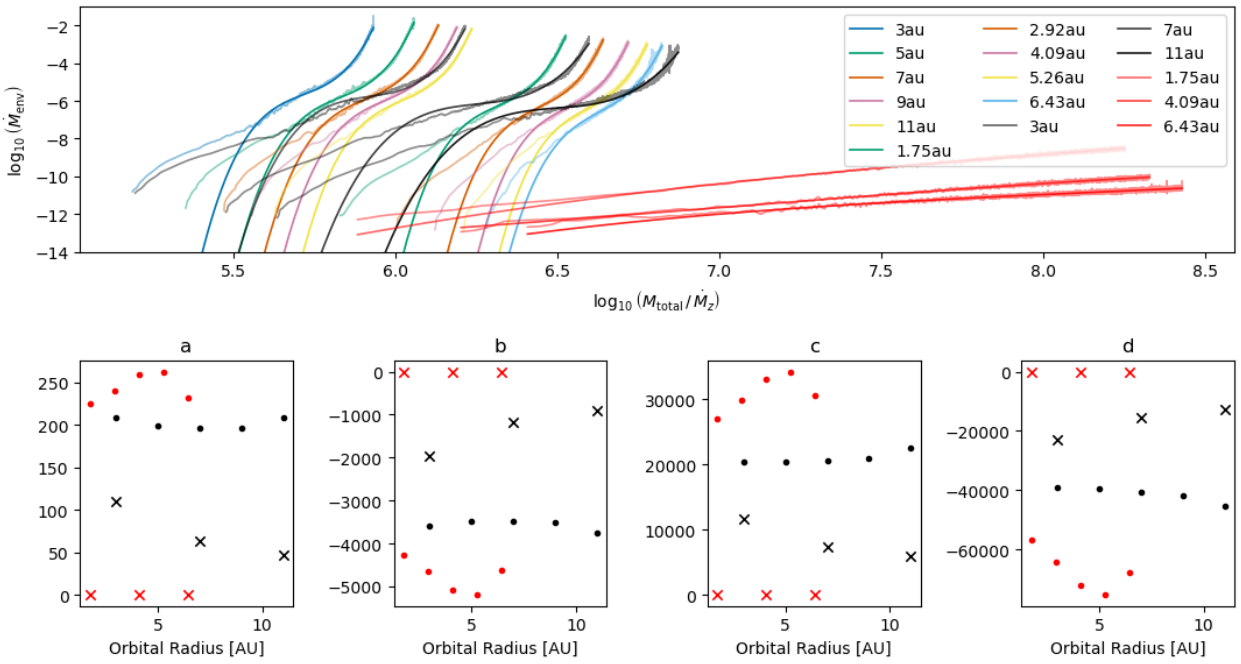

Figure 20: The best fit polynomial applied to both non-evolving and evolving cases. The coefficients of best polynomial fit are shown, however indicate no obvious or straightforward way to predict them. Evolving disks are denoted by a crossed marker, while non-evolving disk cases are denoted by a dotted marker. Planets forming around solar type stars are in black, while those around M-stars are in red.

In our search for a fitting function for the total mass divided by the solid accretion rate, rather than pursuing a complicated procedure of trying to accurately predict these coefficients for the different cases, we can pursue another method. We implement a best fit to the data

at a given reference point, 7 astronomical units around a G-type star, and then correct our fit based on correction factors for the orbital separation and stellar mass. In essence, a polynomial fit equation would be of the form

$$\dot{M}_{\rm env} = \left(\dot{M}_{\rm env,7AU,1M_\odot}\right)\left(\frac{r}{7\rm AU}\right)^{\alpha}\left(\frac{M}{1\rm M_\odot}\right)^{\beta}, \tag{63}$$

$$\Rightarrow \log_{10}\left(\dot{M}_{\rm env}\right) = \log_{10}\left(\dot{M}_{\rm env,7AU,1M_\odot}\right) + \alpha\log_{10}\left(\frac{r}{7\rm AU}\right) + \beta\log_{10}\left(\frac{M}{1\rm M_\odot}\right), \tag{64}$$

where the value of $\log_{10}\left(\dot{M}_{\rm env,7AU,1M_\odot}\right)$ is given by the polynomial fit of equation (62).

The implementation of this equation would result in the shifting of the fit for the data at 7 AU around a G-type star, depending on the orbital separation and the host star mass. The amount by which the reference fit is shifted is given by the fitting of the exponents α and β. How these are fitted depends on the method by which the reference fit is shifted. We investigate here two separate methods, *horizontal* shifting and *tilted* shifting.

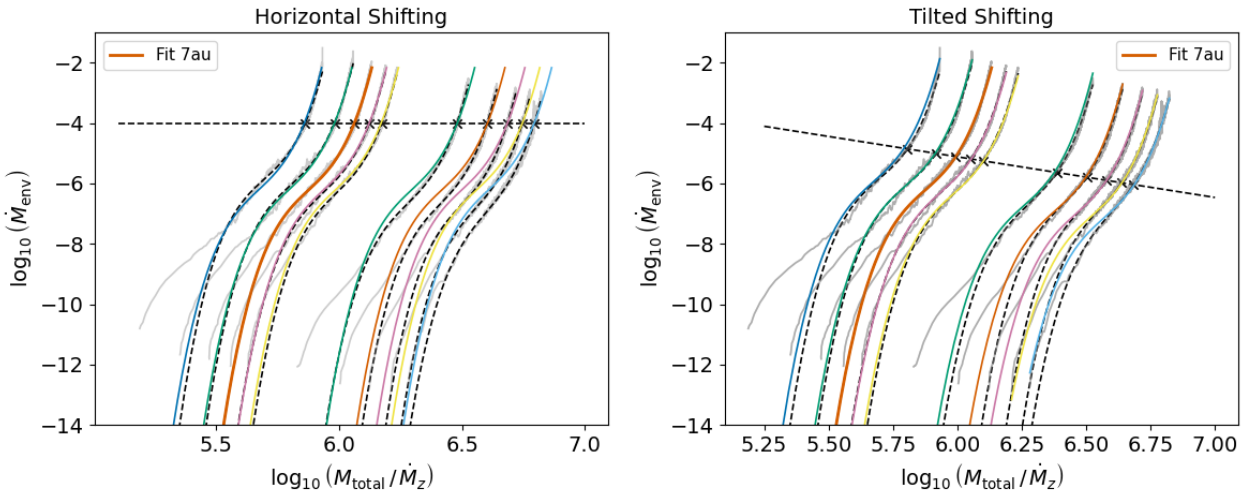

Figure 21: Two methods of shifting a fitted polynomial using radial and stellar mass correction factors.

Horizontal Shifting

The concept of horizontal shifting refers to shifting the solution at 7 AU and 1 solar mass along a horizontal line and by an amount determined by a fitting function which takes the orbital separation and stellar mass into account. As shown in the left hand panel of figure 21, we choose an ordinate axis value we think is appropriate in order to act as the guide line to fit the α and β coefficients of equation (64). We choose a gas accretion rate value of $10^{-4}\rm M_\oplus/yr$ since it connects well dense regions of the gas accretion rates and reaches values over all cases, rendering it a suitable guide line value. Taking the points on this guideline

which correspond to the best fit polynomial values for each case, we fit equation (64) and obtain

$$\alpha = 0.5543\,, \qquad \beta = -1.0769\,. \tag{65}$$

Figure 21 shows the unique polynomial fits in dashed black lines and the shifted polynomial fits in colour. The mean weighted root mean square of these fits is given as

$$\text{WRMS} = 0.434\,, \tag{66}$$

indicating a good agreement with data and an improvement on the previously fitted function of equation (60).

Tilted Shifting

Another method of performing the polynomial fit takes a slightly different tack and uses a *tilted* guideline to perform the corrective fit. We recognise that horizontal shifting does not capture the natural movement of the polynomials over radius and stellar mass. As shown in the right hand panel of figure 21, there exists a natural curvature in the data, with the movement of the curvature point decreasing from left to right in the figure. This curvature point defines the spine of the data and we choose to fit a line with a non-zero slope through these points, to act as the guideline for the fitting procedure. From fitting a line through points fitted by visual inspection, we obtain a tilted guideline with slope and intercept given as

$$m = -1.3485\,, \qquad c = 2.9774\,. \tag{67}$$

In this method, we take a given independent variable point, then shift it along the tilted line by an amount determined by a fitting function in order to reach the corresponding independent variable point for the polynomial at 7 AU and 1 solar mass. We then calculate the gas accretion rate and shift the calculate point back along the tilted line. With this method we find the optimum tilt-shifting parameters to be

$$\alpha = -0.5478\,, \qquad \beta = 1.0201\,, \tag{68}$$

where the signs now indicate we decide to shift from a given orbital separation and stellar mass to the polynomial at 7 AU and 1 solar mass, rather than the other way around, as was done in the horizontal fitting. We also note for completeness that the optimum polynomial fit parameters for the fit in $\log_{10}$ space for 7 AU and 1 solar mass are

$$a = 123.9105\,, \quad b = -2184.3115\,, \quad c = 12842.7464\,, \quad d = -25190.9544\,, \tag{69}$$

corresponding to equation (62).

The mean of the weighted root mean squared value for this method is given as

$$\text{WRMS} = 0.248\,, \tag{70}$$

which indicates a very good agreement with data an a superior fit to the horizontal shifting method. The improvement comes from recognising that the shape of the fitted polynomial

moves vertically as well as horizontal, rendering a mere horizontal fit insufficient.

We can now apply our tilt shifting polynomial fit carefully to the data and assess the quality of the fit. In figure 22 we cut the MESA data to a relevant range, which naturally changes the weighted root mean square value slightly, and overlay the fit. Visually, we see a very good agreement with the MESA data, where the predicted growth tracks follow closely the simulated gas accretion rates. This is in agreement with the weighted root mean squared values in table 5, where we see the low total average using the tilted shifted polynomial method. This represents not only an improvement on the horizontal shifting method but also on the model by Eriksson et al. (2023) [40].

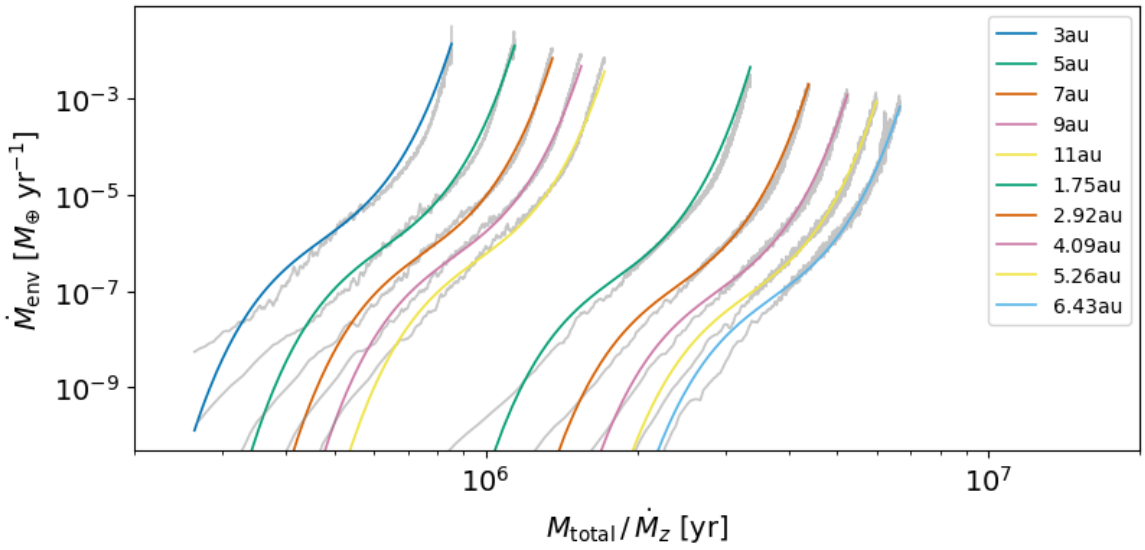

Figure 22: Applying the tilted polynomial fitting method to the data.

The inclusion of evolving disk cases is, however, more complicated to include with this polynomial fitting method. As seen in figure 20, the growth trajectories for evolving cases, and their corresponding polynomial fit coefficients, can vary very significantly from the non-evolving disk cases. This highlights a limitation of the model in that it only applies to a select few physical cases and is difficult to generalise to other cases. Combining this fact with a weighted root mean squared value which represents a good but not excellent improvement over the fit by Eriksson et al. (2023) [40], can we find another fitting function which is more robust over different physical setups and which represents a significant improvement over the fit by Eriksson et al. (2023) [40], justifying its use? This is the focus of the next section.

4.2.3 A New Approach

We know from table 4 that a polynomial fit represents an improvement to the fitting the gas accretion rates, although, considering table 3, the improvement may not be enough to justify its use. Combining this with issues of robustness over different physical cases, we look

Star Mass [$M_\odot$]	Orbital Radius [AU]	WRMS	Avg. WRMS	Total Avg. WRMS
1	3	0.3190	0.408	0.291
1	5	0.4429		
1	7	0.5125		
1	9	0.4440		
1	11	0.3191		
0.2	1.75	0.3595	0.174	
0.2	2.92	0.1769		
0.2	4.09	0.1105		
0.2	5.26	0.0996		
0.2	6.43	0.1215		

Table 5: The weighted root mean square values for the fitting function from the **tilted polynomial fit**.

for a different gas accretion fitting method. We wish to find a method which is robust over different physical cases and which is accurate in its predictions.

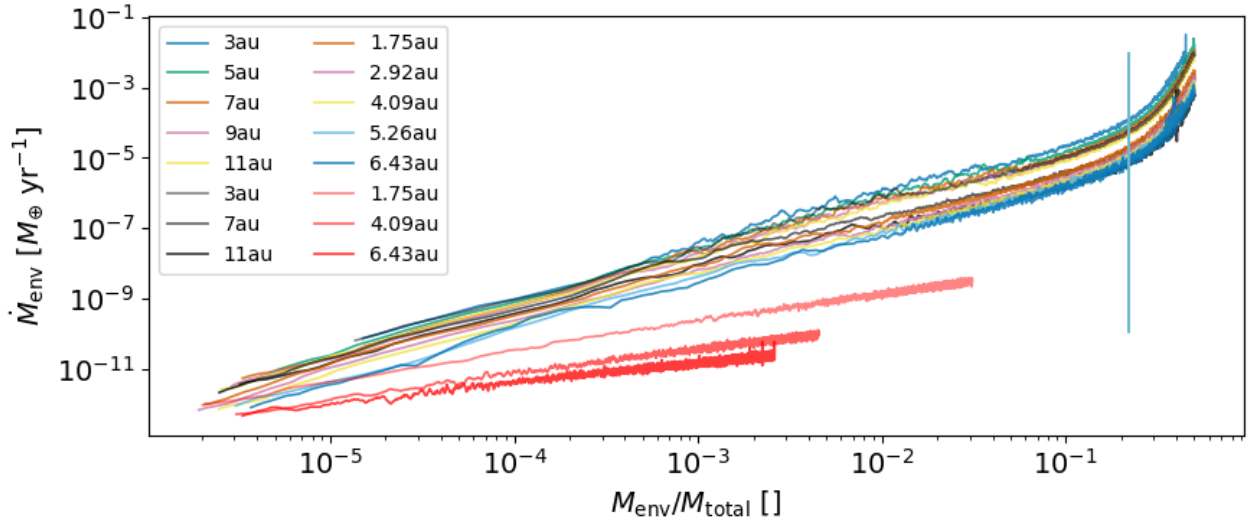

Figure 23: The gas accretion rate as a function of the envelope mass divided by the total mass of the planet. The evolving M-disk cases are in red. The behaviour over all cases, excluding the evolving M-type disk cases, exhibit similar characteristics. The transition between growth regimes occurs at the same point across the cases. The vertical lines denote the point where the envelope mass fraction is 0.22 with the gas accretion behaviour at this point similar over all cases.

We make two observations which lead us toward a new method for a gas accretion fitting

equation. The first is shown in figure 23, a plot of the gas accretion rate as a function of the envelope to total mass ratio. For all cases which reach crossover mass, we notice that they exhibit the same behaviour, or general shape, and shift only vertically due to a difference in gas accretion rates. We recognise that a significant increase in the gas accretion rates occurs at the same envelope to total mass ratio for all cases. The vertical line shown in the figure represents the point where the ratio is 0.22. This also represents two inherently different growth regimes, demarcated by the point where the ratio is about 0.22, which we denote as the *breakpoint*. This breakpoint defines a natural transition between two separate growth regimes and is chosen by trial and error.

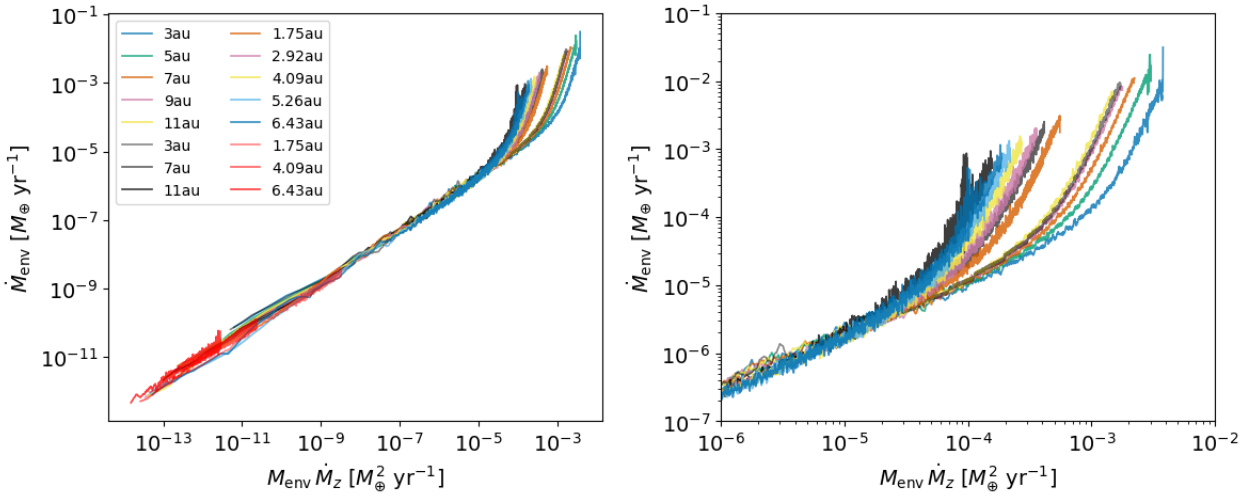

Figure 24: A new variable to consider, namely the envelope mass times the solid accretion rate. The gas accretion rates over this variable follow regular behaviour for all the considered cases, including evolving and non-evolving disks.

Our second observation is shown in figure 24 where we plot the gas accretion rates for all cases considered over a newly considered variable, namely the envelope mass multiplied by the solid accretion rate. Astonishingly, we notice that the growth tracks all lie on top of each other until a certain point where they break off into accelerated growth tracks, all with a similar shape. The right hand panel in this figure is a zoomed-in plot of the enhanced growth regime. The gas accretion rates continue on the main spine until a certain point, at which they experience accelerated gas accretion rates. The differences between these tracks show a regular behaviour, leading us to believe that they could offer a method of predicting gas accretion rates.

The variable $M_{\rm env}\,\dot{M}_z$ presents itself as a very useful independent variable over which to plot the gas accretion rates, given the robustness of the behaviour across the cases considered. The value is monotonically increasing over time, for both non-evolving and for evolving disk cases. This behaviour was not observed for other independent variables, such as the total mass divided by the solid accretion rate, and highlights this new variable as a very useful candidate over which to fit the gas accretion rates. This monotonically increasing behaviour

is a result of the regulation of the solid accretion rate by multiplying by the envelope mass, which the gas accretion rate is a strong reflection of. Since the simulations follow the same growth tracks, we see that the combination of the envelope mass and the solid accretion rate describes very robustly the gas accretion in the early stage of growth, without need for other terms. This variable is also very useful because it is analytically predictive. The solid accretion rate is given by the pebble accretion rate, which is merely a function of the total planet mass, stellar mass and orbital radius, assuming that the gas and solid disk parameters are already defined. This makes the usage of $M_{\rm env}\,\dot{M}_z$ as a predictive variable very tangible.

Our goal is to combine these two observations in a way which allows us to fit and predict the gas accretion rates in a robust and accurate manner. Essenitally, we wish to now perform a fit of the gas accretion rates, $\dot{M}_{\rm env}$, as a function of this new variable, $M_{\rm env}\,\dot{M}_z$.

Linear Blend Function

Recognising two separate growth regimes in figure 24, we opt to fit the left hand and right hand growth regimes with linear fits and then stitch our solutions together. In order to perform this, we need to determine two things. Firstly, we need to determine the transition point between the two linear growth regimes. Secondly, we need a way of continuously stitching together our two separate solutions in order to arrive at a single, continuous solution.

The transition between the two regimes, or the *breakpoint*, is chosen from the findings of figure 23. From trial and error, we choose to define the breakpoint as the point where the envelope to total mass ratio is 0.22. From our MESA results, we can determine the values of $M_{\rm env}\dot{M}_z$ for which the envelope to total mass ratio is 0.22, which we can use to fit the following breakpoint prediction

$$\log_{10}(M_{\rm env}\dot{M}_z)_{\rm BP} = \alpha + \beta\log_{10}\left(\frac{M_*}{M_\odot}\right) + \gamma\log_{10}\left(\frac{r}{1\text{AU}}\right)\,, \tag{71}$$

where the stellar mass and orbital separation are given in solar masses and astronomical units. The results of this fit are presented as

$$\alpha = -2.6218\,, \qquad \beta = 1.6307\,, \qquad \gamma = -0.8966\,. \tag{72}$$

The breakpoints are shown in the first panel of figure 25. The breakpoints mark the points of transition between the thwo phases of growth. We can assess the accuracy of this from the panel in the bottom center of the figure. Here, the breakpoint values from the MESA simulation data are presented on the abscissa axis, while the values from the prediction of equation (71) are plotted along the ordinate axis. The scatter points line up almost perfectly on the 1-1 line, indicating an excellent performance by the prediction equation of the breakpoints. This also indicates that changes of the breakpoint over orbital radius and stellar mass are fully accounted for by these two factors, meaning there are no additional parameters at play influencing the values of the breakpoints. Again, we only consider non-evolving disks here. Additional considerations are required in the case of evolving disks.

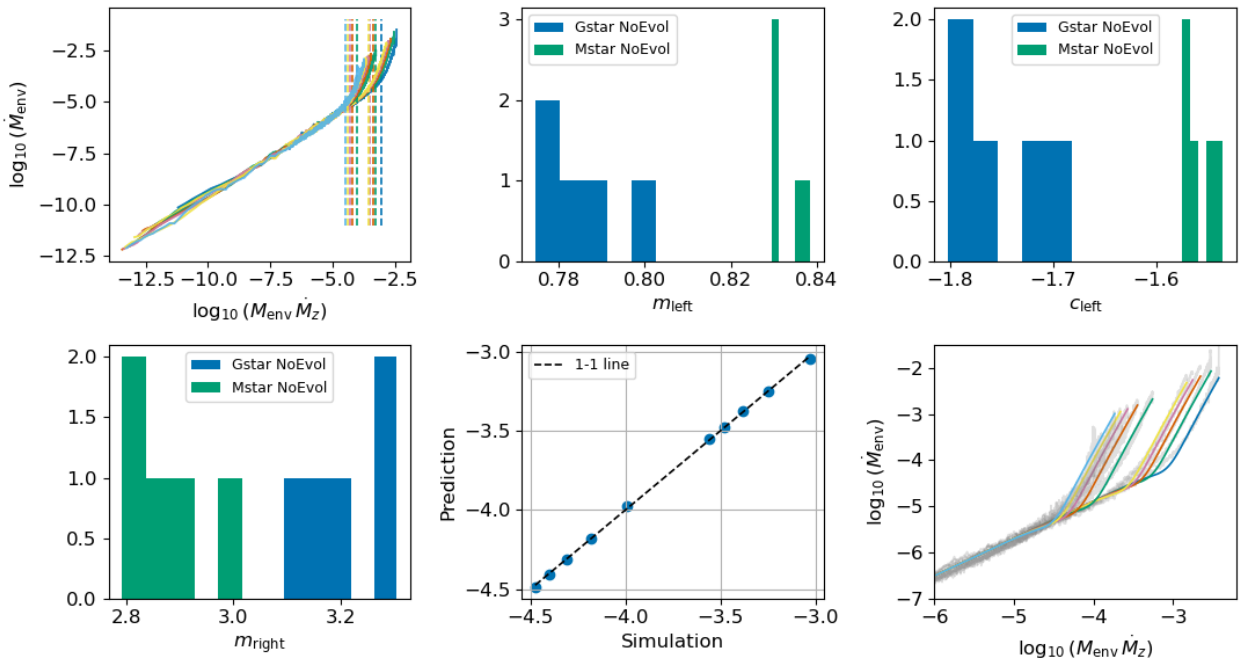

Figure 25: The linear blend function performed and implemented using an envelope to total mass ratio of 0.22, using only the non-evolving disk cases. The ratio value defines the breakpoints, and are plotted as vertical lines in the first panel. Straight lines are fitted to the data to the left and right of the breakpoints, with slopes and intercept plotted as histograms. The breakpoint is predicted with excellent accuracy and compared with simulation data. Lastly, we see that fitted gas accretion function from the linear blend method.

Given accurate values of the breakpoints which distinguish the two growth regimes, we can move forward by performing linear fits on the left and right hand data. The values of the slopes and intercepts are plotted for the G-star and M-star data in histograms in figure 25. Note that the intercept value of the right hand side data is not needed since we can attach our two solutions at the breakpoint, already determined by our prediction equation. The corresponding ordinate value is given by the fit of the line from the left hand side data, evaluated at the breakpoint. From the histograms, we note a spread in the values of the slopes and intercept over stellar mass. This presents an additional complication. Rather than pursuing extra fitting functions to determine the dependence of the slopes and intercept on orbital separation and stellar mass, we take an average of the given values and apply these values to all cases in our predictions. Although we lose some accuracy through averaging, this is justified since the range of values for the slopes and intercept are relatively narrow. With this is mind, we present the averages as

$$m_{\text{left}} = 0.809\,, \qquad c_{\text{left}} = -1.654\,, \qquad m_{\text{right}} = 3.039\,. \tag{73}$$

Now that we have a method of determining the breakpoints and we have values for the two linear fits, we need a method to smoothly stitch together the solutions at the breakpoint. We choose to use a blending function, powered by a sigmoid function, which is a shifted logistic

curve, to smoothly blend the linear solutions. We define the sigmoid function as

$$\sigma(x, k, x_0) = \frac{1}{1 + \exp\left[-k(x - x_0)\right]}\,, \tag{74}$$

which smoothly transitions between the values 0 and 1 at a point x_0 over a range defined by a smoothing parameter k, defining how quickly the transition is. The blending function can thus be defined as

$$f(x) = (1 - \sigma(x))\left[m_1 x + c_1\right] + \sigma(x)\left[m_2 x + c_2\right]\,. \tag{75}$$

In figure 26 we plot toy examples of these two functions for varying values of the smoothing parameter k. The left hand panel shows the sigmoid function, where x_0 is defined to be zero. The sharpness, or efficiency, of the transition is determined by k. A low value of k would make the transition between two values very gradual and inefficient, however too high a value presents unphysical behaviour and can results in discontinuous jumps or a function which is not continuously differentiable. An intelligent choice of k is required for each unique application. In the second panel, we see an example of the sigmoid powered blending function, where we stitch together two straight lines of arbitrary slope and intercept for varying values of k. The efficiency of the transition becomes much more favourable for higher values of k. The resulting function blends together the two linear lines at the transition point in a continuous and continuously differentiable manner.

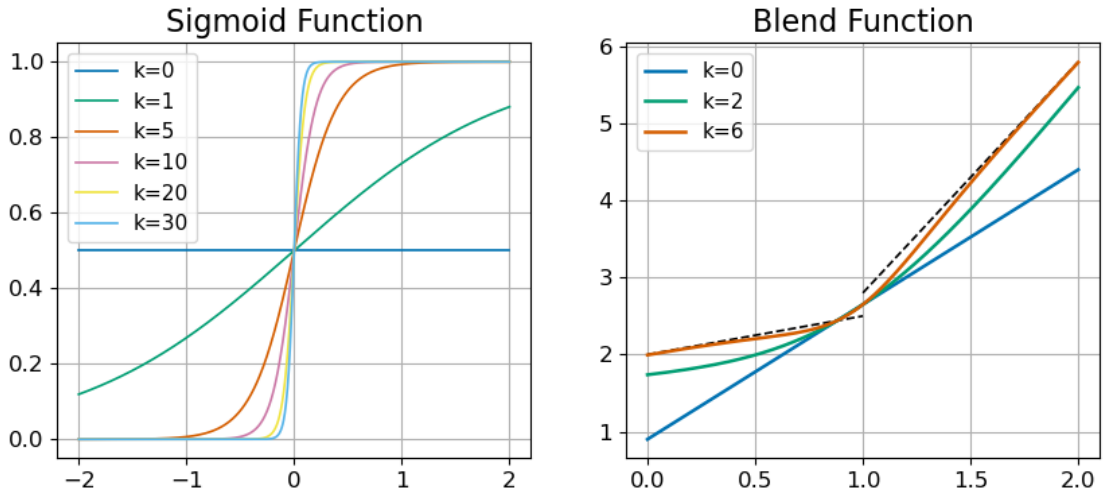

Figure 26: The sigmoid function for different values of k, the smoothing parameter. The linear blend function is also shown. Two arbitrary straight lines with a discontinuous break are plotted in dashed black, with the linear blend function used to stitch them together for different values of k. The result is continuous and continuously differentiable.

Using the values obtained, we define the linear blend function as

$$\log_{10}\left(\dot{M}_{\rm env}\right) = (1 - \sigma(x, k, x_{\rm BP}))\left[m_{\rm left} x + c_{\rm left}\right] + \sigma(x, k, x_{\rm BP})\left[m_{\rm right} x + x_{\rm BP}(m_{\rm left} - m_{\rm right}) + c_{\rm left}\right]\,, \tag{76}$$

where x is our new variable $\log_{10}\left(M_{\text{env}}\dot{M}_z\right)$, the breakpoints x_{BP} are obtained from equation (71), the slopes and intercept obtained from equation (73) and the value of k chosen as 10. The results of this procedure are shown in figure 27 where we show the applied function over the whole data range and where we zoom into the region around the breakpoints. Visually, we note that there exists a very good agreement between the prediction and data, with the predictions tracking the data closely. This is confirmed by the results of the weighted root mean squared in table 6, where the total average is 0.124, a significant improvement upon the previously attempted fits.

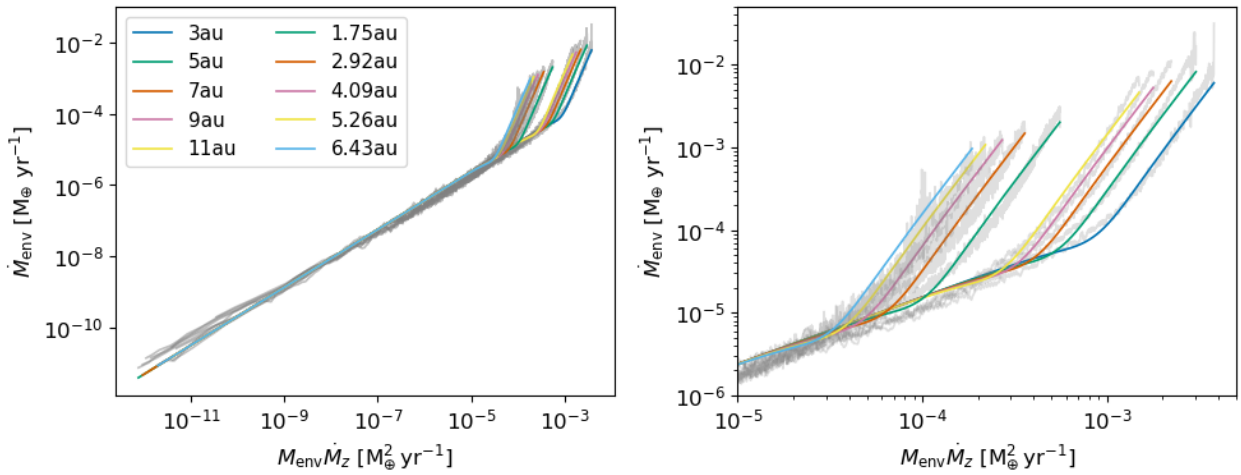

Figure 27: The linear blend function applied to the data. The fit tracks the growth trajectories from the simulations quite well.

Star Mass [$M_\odot$]	Orbital Radius [AU]	WRMS	Avg. WRMS	Total Avg. WRMS
1	3	0.1102	0.104	0.124
1	5	0.1069		
1	7	0.0985		
1	9	0.1008		
1	11	0.1053		
0.2	1.75	0.1202	0.143	
0.2	2.92	0.1262		
0.2	4.09	0.1400		
0.2	5.26	0.1603		
0.2	6.43	0.1685		

Table 6: The weighted root mean square values for the fitting function from the **linear blend function**.

We note, however, that this linear blend fit is not entirely accurate and presents some approximations. The growth trajectory of the gas accretion rate over the variable $M_{\text{env}}\dot{M}_z$ exhibits some curved behaviour within the two distinct growth regimes, rendering linear approximations as not entirely accurate. The variation of the linearly fitted slopes and intercept in figure 25 also suggest that linear fitting may not be wholly appropriate for the prediction of the gas accretion rates. We now shift our focus to the final investigated fitting procedure, the *polynomial blend function*, where we aim to stitch together polynomials in each growth regime rather than linear functions.

Polynomial Blend Function

The variation in the slopes and intercepts of the linear blend function applied to the data suggest it is not wholly appropriate to use, rather acting as a sufficient approximation. We opt to improve our blending function fit by stitching together two separate polynomials. Upon investigating figure 24 a little more closely, we choose to perform a single third order polynomial fit to the data left of the breakpoint and a predictive second order polynomial fit for each individual case for the right hand side of the break point. Higher accretion rates are more important, so we choose to perform individual predictive fits for the right hand side, while lower accretion rates are less important so we allow ourselves to perform a single polynomial fit.

In figure 28 we shift the data such that the breakpoints for each individual case lie at the origin. The data also line up very nicely on top of each other, with the data left of the breakpoint overlapping very strongly, while the data right of the breakpoint presents only a slight change over orbital separation and stellar type. This reveals a common, unified behaviour of the gas accretion rates once we line them up over their breakpoints, making the accurate prediction and use of these breakpoints all the more important. There also exists a slight curvature in the data on the left hand side of the breakpoint, meaning that a polynomial fit would be appropriate to capture the behaviour in this region. The curvature of the data to the right hand side of the breakpoint, along with the slight shifting over parameters, suggests a unique polynomial fit for each case, to capture the slight differences.

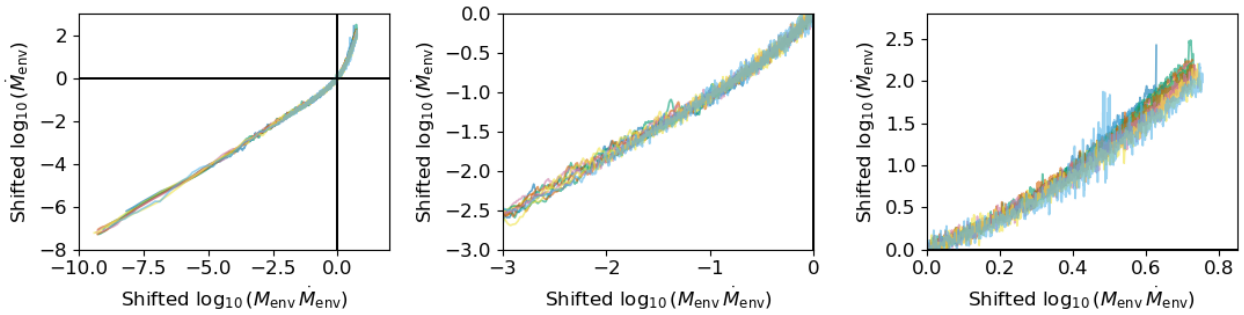

Figure 28: Shifting the data such that the breakpoints line up at the origin. By visual inspection, we see that the data overlap nicely left of the breakpoint and diverge slightly right of the breakpoint. The data is plotted in $\log_{10}$ space.

We choose to perform a third order polynomial fit for the data on the left hand side of the breakpoint and a second order polynomial fit for the data on the right hand side. The third order polynomial captures the slight curvature changes which make the linear fit from the last section not wholly appropriate whereas a second order polynomial is deemed sufficient for the right hand side data. Additionally, we perform a fit to predict the curvature coefficient in the second order polynomial. We deem this sufficient to capture the changes over the orbital separation and stellar mass. More specifically, we first perform a full fit of the polynomial blend function over the whole dataset with breakpoints shifted to the origin, given as

$$\log_{10}\left(\dot{M}_{\rm env}\right) = (1-\sigma(x,k,x_{\rm BP}))\left[a_1x^3+b_1x^2+c_1x\right]+\sigma(x,k,x_{\rm BP})\left[a_2x^2+b_2x\right]\,, \tag{77}$$

where the function is designed to run through the breakpoint. The full fit allows us to extract the coefficients a_1, b_1, c_1 and b_2, which will be used in the final fitting function. We do not need to use the value a_2 since we perform another fit to predict this value based uniquely on the system properties. The full fit is nonetheless shown in the first panel of figure 29. The results of this fit are given as

$$a_1 = 0.0078\,, \quad b_1 = 0.1068\,, \quad c_1 = 1.1307\,, \quad a_2 = 1.5905\,, \quad b_2 = 1.7021\,. \tag{78}$$

The middle panel of figure 29 shows the best fit second order polynomial to the right hand side data, weighted by the sigmoid function term. Specifically, the optimum coefficients are found for the equation

$$g(x) = \left(\frac{1}{1+\exp(-kx)}\right)\left(ax^2+b_2x\right)\,, \tag{79}$$

where again x is the variable $\log_{10}\left(M_{\rm env}\dot{M}_z\right)$ shifted by an amount equal to the breakpoints. The value b_2 is taken from the full fit of the polynomial blend function, given in equation (78). We are specifically only fitting for one parameter here in equation (79), a, which describes the curvature of the fit. The fitting equation used again employs radial and stellar mass correction terms and is given as

$$a_{\rm fit} = a_a + b_a\log_{10}\left(\frac{r}{1{\rm AU}}\right) + c_a\log_{10}\left(\frac{M}{1{\rm M}_\odot}\right) \tag{80}$$

with the results of the fitting procedure using the values from the best fit given as

$$a_a = 2.5380\,, \quad b_a = -0.6933\,, \quad c_a = 0.9129\,. \tag{81}$$

The results of this prediction are shown in the last panel of figure 29. We note a reasonable performance of the fit and a sufficient accuracy with the best fits using the simulation data. The trend over orbital radius and stellar mass is captured well, with higher curvature for closer radii to a higher mass host star. The imperfection of the fit suggests that more information is possibly needed, rather than just the orbital radius and stellar mass.

We know have a method of predicting the gas accretion rate for the data shown, however we must remember that we had shifted the data such that the breakpoints line up at the origin.

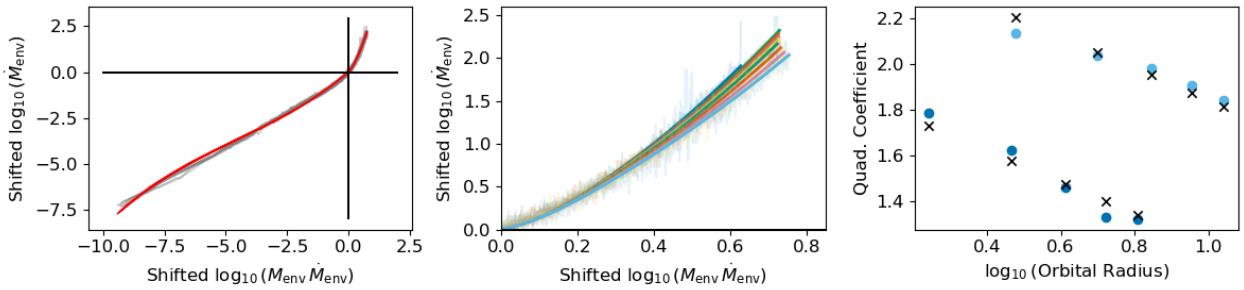

Figure 29: The full sigmoid fit for the polynomial blend function. The polynomial coefficients for the left hand side of the break point are extracted from the full fit. The best second order polynomial fit is plotted for each case in the middle panel. These are used to fit a prediction equation to predict the quadratic coefficient, with the prediction against the best fit values shown in the last panel. The predicted values are given by the black, crossed markers. The results for M-stars are in dark blue, whereas light blue shows the results for G-stars.

In order to shift the predictions back to their physical values, we need to be able to predict the breakpoints. The equation is again similar to previous correction fits, given as

$$\mathrm{BP}_{\mathrm{x/y}} = a_{\mathrm{x/y}} + b_{\mathrm{x/y}} \log_{10}\left(\frac{M_*}{1\mathrm{M}_\odot}\right) + c_{\mathrm{x/y}} \log_{10}\left(\frac{r}{1\mathrm{AU}}\right) , \tag{82}$$

with the results given as

$$\text{x point:} \quad a_{\mathrm{x}} = -2.6218\,, \quad b_{\mathrm{x}} = 1.6307\,, \quad c_{\mathrm{x}} = -0.8966\,, \tag{83}$$

$$\text{y point:} \quad a_{\mathrm{y}} = -3.5663\,, \quad b_{\mathrm{y}} = 1.3832\,, \quad c_{\mathrm{y}} = -0.7532\,, \tag{84}$$

and the scatter plots with data shown in figure 30. The agreement with the breakpoint values from simulations is excellent, illustrating that thee polynomial blend function can be used as a means of predicting the gas accretion rates.

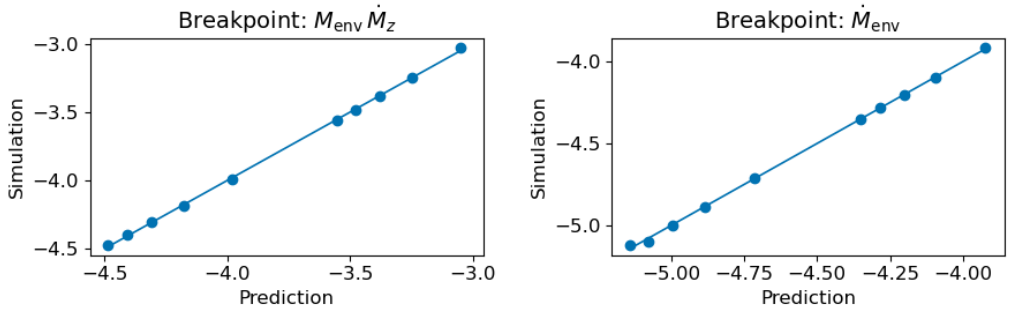

Figure 30: The comparison between the breakpoint values from the MESA simulations and from the predictions. The predictions are obtained by fitting functions dependent on orbital separation and stellar mass. The predictions agree very well with data.

The full equation to predict the gas accretion rates using the polynomial blend function is

thus given as

$$\begin{aligned}\log_{10}\left(\dot{M}_{\rm env}\right) = &\left[1-\sigma(x,k,x_{\rm BP})\right]\left[\alpha_1(x-x_{\rm BP})^3+\beta_1(x-x_{\rm BP})^2+\gamma_1(x-x_{\rm BP})\right]\\ &+\left[\sigma(x,k,x_{\rm BP})\right]\left[\alpha_{2,\rm fit}\left(r,M_*\right)(x-x_{\rm BP})^2+\beta_2(x-x_{\rm BP})\right]+y_{\rm BP}\,,\end{aligned} \tag{85}$$

for $x=\log_{10}\left(M_{\rm env}\dot{M}_z\right)$ and where the function σ is defined as

$$\sigma(x,k,x_{\rm BP}) = \frac{1}{1+\exp\left[-k(x-x_{\rm BP})\right]}\,. \tag{86}$$

The function $\alpha_{2,\rm fit}$ is from equation (80) and is given as

$$\alpha_{2,\rm fit}\left(r,M_*\right) = a_a + b_a\log_{10}\left(\frac{r}{1\rm AU}\right)+c_a\log_{10}\left(\frac{M_*}{1\rm M_\odot}\right)\,. \tag{87}$$

The breakpoints are from equation (82) and repeated here as

$$\rm BP_{x/y} = a_{x/y}+b_{x/y}\log_{10}\left(\frac{M_*}{1\rm M_\odot}\right)+c_{x/y}\log_{10}\left(\frac{r}{1\rm AU}\right)\,. \tag{88}$$

The parameters for the fits are given in table 7

Parameter	Value	Parameter	Value
α_1	0.0078	$a_{\rm x}$	-2.6218
β_1	0.1068	$b_{\rm x}$	1.6307
γ_1	1.1307	$c_{\rm x}$	-0.8966
a_a	2.5380	$a_{\rm y}$	-3.5663
b_a	-0.6933	$b_{\rm y}$	1.3832
c_a	0.9129	$c_{\rm y}$	-0.7532
β_2	1.7021	k	10

Table 7: Values for parameters used in the full polynomial blend gas accretion fit.

Finally, in figure 31 we implement out polynomial blend fit to the data. We see an excellent agreement with the simulation data. The left hand side polynomial tracks the data excellently, leaving the prediction at the breakpoint. The right hand side data then captures the curvature of this part of the data, a far superior fit than approximating the data as linear. We see the weighted root mean squred values in table 8. The total weighted root mean squared value of 0.083 indicates an excellent agreement with data.

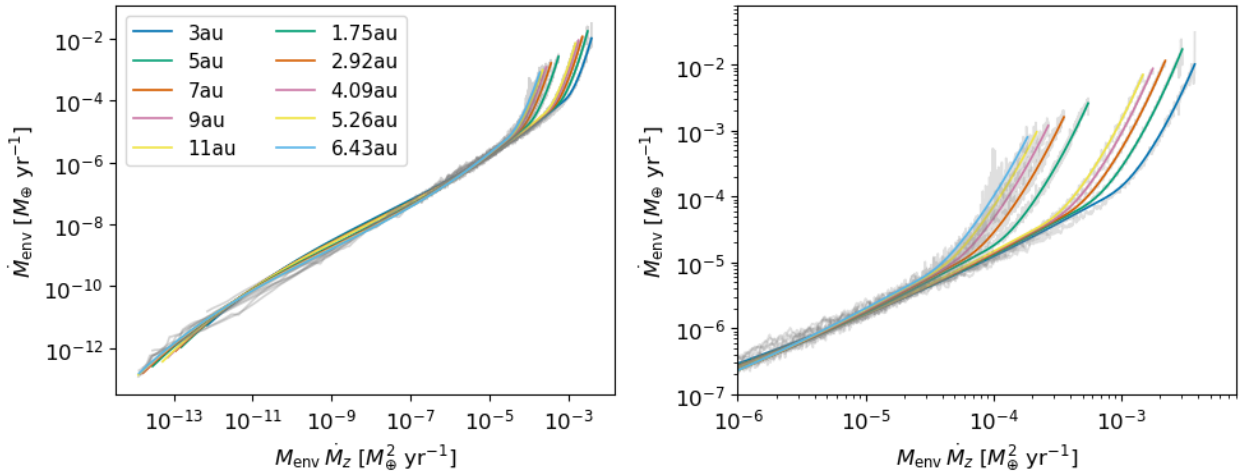

Figure 31: Applying the polynomial blend function, including the prediction for the curvature of the data after the breakpoint, results in an excellent agreement with data. The right hand panel shows a zoom in on the data close to crossover.

Star Mass [$M_\odot$]	Orbital Radius [AU]	WRMS	Avg. WRMS	Total Avg. WRMS
1	3	0.1056	0.098	0.083
1	5	0.0927		
1	7	0.0952		
1	9	0.0954		
1	11	0.1022		
0.2	1.75	0.0529	0.068	
0.2	2.92	0.0587		
0.2	4.09	0.0612		
0.2	5.26	0.0739		
0.2	6.43	0.0933		

Table 8: The weighted root mean square values for the fitting function from the **polynomial blend function**.

4.2.4 Comparison with Simulation Data

We can compare the performance of the gas accretion fits in figure 32. The solid accretion rates, as well as the investigated gas accretion fits, are implemented in computationally using the PYTHON programming language. We see that the polynomial blend fit consistently performs the best over the cases considered. There is a slight disparity concerning the total mass at crossover due to a slight underestimation of the gas accretion rate from the fit during the simulation. This means that there is less gas accreted during this time, whereas solids are consistently being accreted in the meantime. Therefore the gas needs to catch up on more solid mass before crossover is reached, leading to a higher total mass at crossover. Although

the fit performs very well, this represents an imperfection in the fit, suggesting that different polynomial orders may have been prudent to investigate for the blend function.

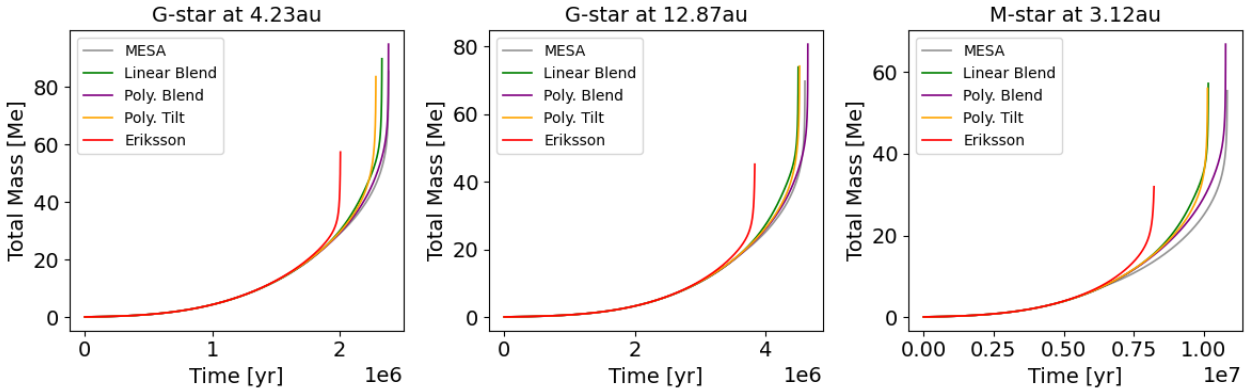

Figure 32: Comparing the investigated fits with the MESA simulation data. The polynomial blend fit provides the best predictions for the data, agreeing very well with the MESA simulations.

4.3 Exploration of Growth Rates

Using the methods of gas accretion developed in the previous section, we can now analyse in more detail the effects of orbital radius and stellar mass on the formation of gas giant planets. We simulate the growth of a range of cases with non-evolving disks, over the stellar masses 0.2, 0.6, 1 and 1.4 solar masses, as well as a variety of orbital radii, corresponding to 2, 6, 10 and 14 around a solar mass star. The radii across the other stellar masses are chosen in each case such that the orbital period is equal, leading to the same dynamical time. In figures 33 and 34 an effective period is given in arbitrary units, where physical constants have been factored out. Similar to the simulations using MESA, the simulations are terminated at the crossover mass.

From figure 33 we see the core mass as a function of time with the specific values presented in table 9. The core mass given at crossover increases as the host star mass increases and as the orbital separation between the planet and the host star decreases. The change in crossover core mass over stellar type is stronger for closer orbital separations but then becomes weaker as the orbital separation increases. The difference between the core masses at crossover for the highest and lowest mass stars considered at the closest orbital radius is approximately 17.6 $M_\oplus$, while the difference for the furthest orbital radii is only 13.3 $M_\oplus$. Conversely, the difference in masses from the closest to furthest orbital period becomes larger for increasing stellar mass. The difference in the case of the 0.2 $M_\odot$ star is 9.3 $M_\oplus$, while the difference for the 1.4 $M_\odot$ star is 13.5 $M_\oplus$.

Figure 34a shows a heatmap of the core masses at crossover for the cases considered as a function of the effective orbital period and the host star mass. The highest core masses

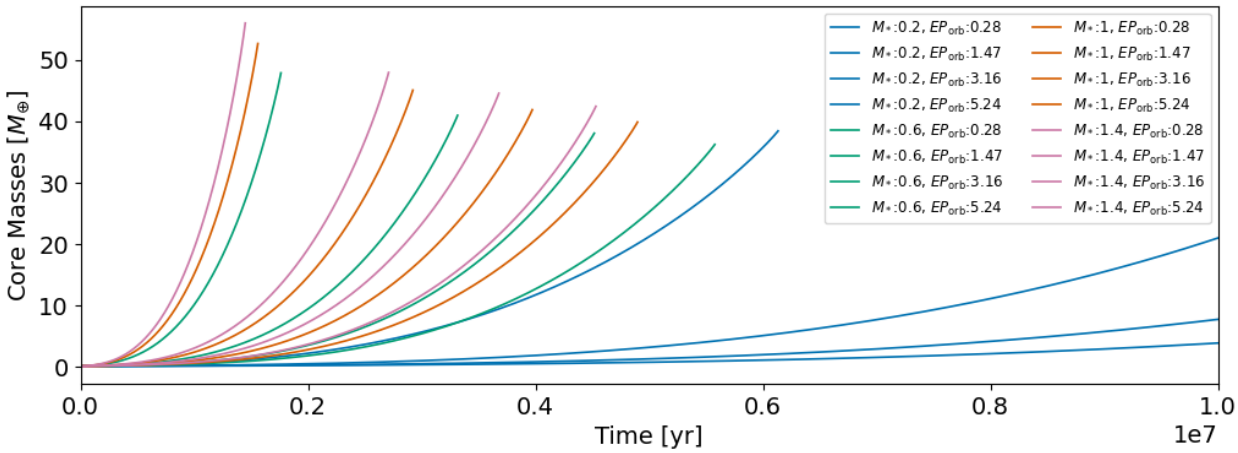

Figure 33: The core mass over time for a selection of cases. The data were generated numerically using the polynomial blend function as the gas accretion model.

Star Mass [$M_\odot$]	Effective Period []	Core Crossover Mass [$M_\oplus$]
0.2	0.28	38.39
0.2	1.46	32.862
0.2	3.16	30.529
0.2	5.23	29.065
0.6	0.28	47.83
0.6	1.46	40.924
0.6	3.16	38.015
0.6	5.23	36.191
1.0	0.28	52.603
1.0	1.46	45.027
1.0	3.16	41.84
1.0	5.23	39.841
1.4	0.28	55.941
1.4	1.46	47.898
1.4	3.16	44.517
1.4	5.23	42.396

Table 9: The core masses in units of Earth masses at crossover using the simulations with the implemented polynomial blend function.

are found at high stellar masses and at close separations to the host star. This follows our intuition, since pebble accretion rates are higher in these conditions, meaning that more solid material is accreted at a quicker rate, leading to a higher core mass. The total planet mass at crossover is therefore naturally higher in these conditions. The opposite is true of

planets around lower mass stars at further separations. The solid accretion rates are lower, leading to a lower core mass. This has natural consequences for the metallicity of a planet. Since runaway growth occurs around the crossover mass, if the mass of solid material, the core mass, at this point is high, the planet will have a high metallicity upon final formation, after runaway growth is terminated by, for example, a gap opening in the disk. If the planet begins runaway growth with a lower core mass, then it is assumed that the fraction of solid mass at the end of runaway growth will be lower. This results in the conclusion that the metallicity of giant planets around lower mass stars and further away from the star will be lower than otherwise, indicating a positive metallicity gradient with stellar mass and a closer orbital separation. The one caveat to this conclusion is balancing the crossover time with the disk lifetime. If the crossover is reached shortly before the lifetime of the disk, then there may not be enough time for the planet to accrete enough gaseous material to reach a gap opening event, for example, or reduce its metallicity value a lot. Although this is a fine tuning problem, it is still something to keep in mind.

The changing gradients for the core mass at crossover are also reflected in this figure 34a. The change in crossover core mass at closest orbital separation is very slight between the two highest stellar mass cases. The gradient is however much stronger between the two lowest mass stars. This reflects that, at a given effective orbital period, the core mass at crossover rises quickly with changes in stellar mass and then plateaus. Similarly, the core mass at crossover decreases over increasing orbital period, however does so more strongly between close separations rather than distant separations. This reflects a relaxing gradient in the solid accretion rate over orbital distance from the host star, as can be seen in figure 6, indicating that changes in the pebble accretion rate over distance become less with greater distance.

Figure 34b shows the timescales involved with reaching the crossover mass, according to the simulations. We see that the times to crossover mass for stellar masses of approximately 0.5 solar masses or greater are roughly within the estimated times of disk dispersion, within 10 million years at the very longest. Only the innermost orbital separation for the 0.2 solar mass star would be roughly within the disk dispersal time. The planets forming at greater orbital radii around this star have very long timescales, up to 18 million years. The gradient over stellar mass is shallow above this stellar mass threshold, however very sharp below it. The timescale increases sharply in the space between the 0.2 and 0.5 solar mass stars. The gradient over orbital radius is also shallow for the higher mass stars, however increases very strongly for the low mass star. This suggests very tenuous criteria for the formation of gas giant planets around low mass stars, whereas the criteria are more robust around higher mass stars. The sharp transition in timescales between the 0.2 and 0.5 solar mass stars also suggests that there is some minimum criterion for the host star mass in order for a forming planet to reach crossover and runaway growth. Given a trend in planet metallicity at crossover increasing over stellar mass and over decreasing orbital radius, there may also exist a minimum metallicity for a gas giant planet. A metallicity below this value would mean that the gas giant would not form. It is estimated that a planetary embryo in equivalent conditions would form within an average disk lifetime of 4-6 million years around a higher mass star but this formation would not happen around a lower mass star, and that there is a sharp transition mass between the two regimes, which we conclude is approximately 0.5 solar

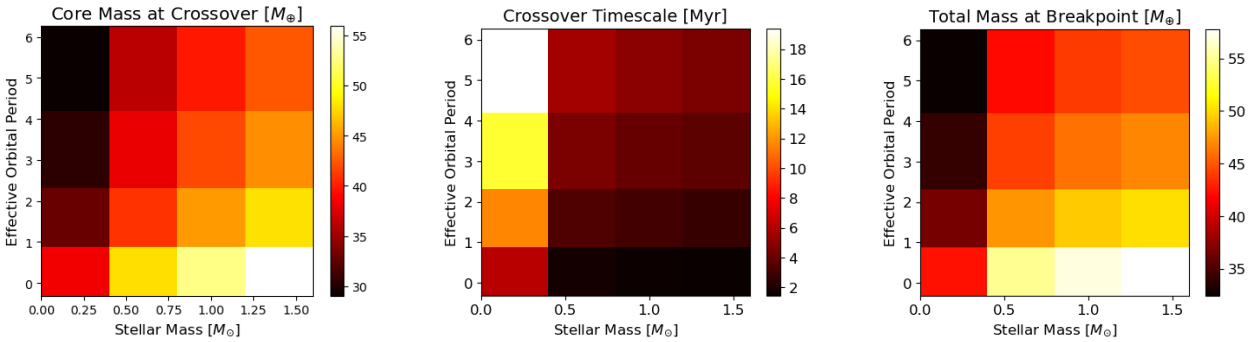

(a) The core mass of the growing planets at crossover in Earth masses. The core mass is higher for a more massive star and for orbits closer to the star. This suggests a growing planet metallicity for these conditions.

(b) The time needed to reach the crossover mass in millions of years. The timescales involved are roughly within the disk lifetime for stars 0.5 solar masses or great, however fall outside of disk lifetimes for less massive stars.

(c) The total mass at the breakpoint value in Earth masses. Visually, we see this correlates with the crossover timescale. Planets which reach crossover have a breakpoint total mass about more than 40 Earth masses.

Figure 34: Results from the simulations with the polynomial blend fitting function. The effects of orbital radius and stellar mass are shown to influence the masses and accretion rates of growing planets.

masses, with forming planets around stars less massive than this unlikely to reach crossover.

Lastly, we see from figure 34c that the total mass of the planet at the breakpoint, where the envelope to total mass ratio is 0.22, increases with increasing stellar mass and decreasing orbital separation. The gradient between the 0.2 and 0.5 solar mass stars is very sharp. We notice that this figure inversely reflects figure 34b, the timescales to reach crossover, which is an indication of whether the giant planet forms or not. We notice the correlation between the two variables, leading us to believe that the total planet mass at the breakpoint value is correlated with the timescale for growth and determines whether the planet reaches crossover within the disk dispersal time. We see from figure 34a that a similar correlation exists for the core mass at crossover, however this is information is not as relevant to predict whether a planet reaches crossover because it uses the crossover value of the core mass itself. Also, as shown in this project, the values of the breakpoint can be predicted using our fitting function, meaning that we can gain insight into the nature of the breakpoint using the fitting functions. Lastly, the gradient for the total mass at breakpoint between the 0.2 and 0.5 solar mass stars is sharper than in the case of the core mass at crossover, indicating that the value is of better use in defining a transition due to its sharpness. We conclude from the figure that planets with a total mass of about 40 Earth masses or less at the breakpoint do not reach the crossover point within the lifetime of the disk.

Our main results can be summarised in figure 35 where we plot the time taken to reach the crossover point as a function of stellar mass. Each line represents a different orbital period, corresponding to different orbital radii. The timescales for growth are very long around low

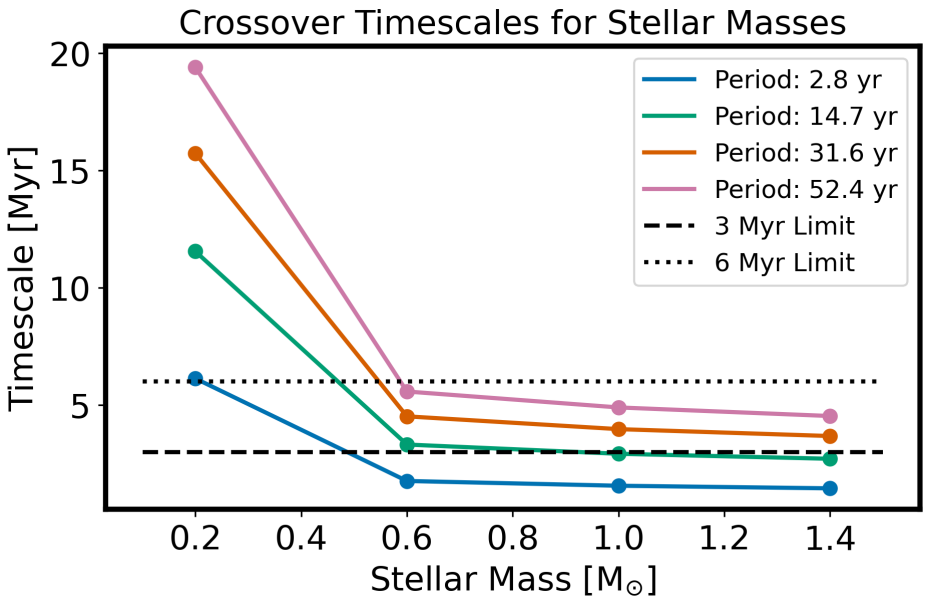

Figure 35: The time taken to reach the crossover mass for a variety of stellar masses and orbital radii. The results are taken from simulations in PYTHON by implementing the equations for the rates of solid and gas accretion. Dashed and dotted horizontal lines indicate possible circumstellar disk lifetimes. The crossover point is tenuously reached below a stellar mass of approximately 0.5 solar masses and robustly reached above it.

mass stars on the order of 0.2 solar masses, however, the timescale drops sharply at the next investigated stellar mass of 0.6 solar masses. The gradient over stellar mass then relaxes and becomes more shallow as the stellar mass is increased. In figure 35 we see two horizontal lines, dashed and dotted, corresponding to disk lifetimes of 3 and 6 million years, respectively, to account for disk lifetime uncertainties. We see that the time to crossover is not reached for low mass stars, however is robustly reached for higher mass stars. We propose a transition point of 0.5 solar masses to differentiate between tenuous and robust giant planet formation.

The results from figure 35 can be compared to observations shown in figure 36, which indicate the occurrence rates of giant planets as afunction of stellar mass [41]. Here, we see a general increase in the observed number of giant planets over increasing stellar mass, supporting our simulation results. This trend is most apparent between stellar masses of 0.6 and 1.2 solar masses, however this deviates below and above these values. This discrepancy can be justified by uncertain disk lifetimes over varying stellar masses. Disk lifetimes are not static, rather vary over the host star properties, even reaching between 5 to 10 million years for brown dwarves [42]. The radiation from the host star could play a role in sweeping away the protoplanetary disk, being swept away quicker from higher mass and stronger radiation stars. In figure 35 we indicate the disk lifetimes as being static and constant over stellar mass, however if we allow the disk lifetime to vary over stellar mass, being longer for lower mass stars and shorter for higher mass stars, we could obtain multiple intersection points between the crossover timescale and the disk lifetime lines. This would mean that there could be some giant planet formation around lower mass stars, due to longer disk lifetimes, and

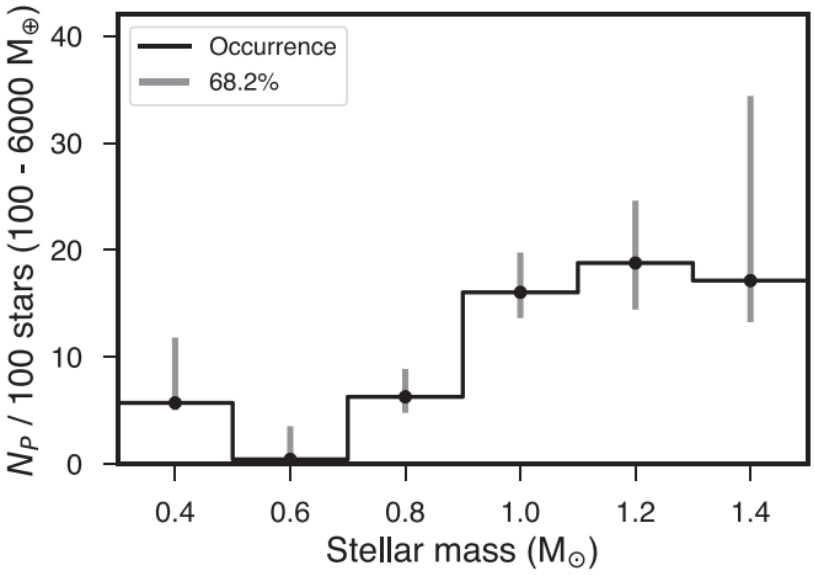

Figure 36: The occurrence rates of giant planets around stars of varying masses. There is a general increase over stellar mass. Adapted from Fulton et al. (2021) [41].

a decrease in giant planet formation around higher mass stars, due to lower disk lifetimes, leading to an explanation for the discrepancies in figure 36.

5 Conclusions

This project investigated the differences in gas accretion rates over different orbital radii around different host star masses. Numerous conclusions were drawn as well as insights gained. It was noted that for a given solid accretion rate, the gas accretion rate increased over increasing orbital radius and over decreasing stellar mass. We reasoned that this was due to a difference in the efficiency of solid accretion rates across the conditions and also due to the fact that the gas accretion rate is a strong function of mass. Since the solid accretion rate for a body of a given mass declines further away from a smaller star, the body's mass needs to be higher in order to have the *same* solid accretion rate as a body closer to a more massive star. However, due to its higher mass, its gas accretion rate is higher. Therefore the gas accretion rate for the same solid accretion rate is higher.

In the course of our investigations we also found a new variable, namely $M_{\rm env}\,\dot{M}_z$, over which the gas accretion rate $\dot{M}_{\rm env}$ exhibits remarkably consistent behaviour across all cases considered, including evolving and non-evolving disk cases, something not seen with other independent variables. The forming planets all follow the same growth track and then break off at different points, what we termed as *breakpoints*. These breakpoints were correlated with another observation, namely that the gas accretion rates as a function of the envelope mass divided by the total mass exhibit similar behaviour and a similar shape, departing into an enhanced growth regimes at a ratio value of approximately 0.22.

Using the newly found variable a new gas accretion fitting function was developed which performed very well, with a weighted mean squared error almost an order of magnitude less than some previous fits. This new fitting function is a *polynomial blend function* with the blending powered by a sigmoid function centered on the calculated breakpoint. This conceptually splits the gas accretion rates into two regimes, a first regime described by a third order polynomial before the onset of enhanced gas accretion rates, at which point the gas accretion rates are described by a second order polynomial with a curvature based on the individual case. The breakpoints and curvature of the second order polynomial are functions of the stellar mass and orbital radius. The accuracy of the gas accretion rate calculations was deemed important since they have an effect on the timescales of growth, on the values of the final masses at crossover and on investigations into parameters such as metallicity. Accurate gas accretion rate calculations are deemed necessary for accurate giant planet formation investigations. There exist, however, caveats with this method of gas accretion fitting. Although the sigmoid powered transition between the two regimes is a smooth one, it introduces an error since the transition is not immediate. Implementing an immediate transition by setting the smoothing parameter, k, to a very high value introduces numerically issues and unphysical behaviour. Also, the fitting of polynomials does not mean that the data is most appropriate for polynomial fitting, rather we have merely chosen to perform this particular fit. Uncertainties can arise given a lack of appropriateness for a given fitting method. There exists a curvature with polynomial fitting which results in the gas accretion rates being slightly underestimated at certain relevant points, leading the a higher core and total mass at crossover. Upon reflection, we conclude that it would have been prudent to investigate the linear blend function more closely, where we attempt to predict the appropriate slopes and intercepts, or where we implement a fit where a linear function blends into a second order polynomial. This removes any unnecessary underestimation of gas accretion rates and, when predicting the fit slopes and intercepts individually for each case, removes the uncertainty involved with averaging the fit to the left of the breakpoint.

We also noted that the gas accretion rates against the variable $M_{\rm env}\,\dot{M}_z$ followed very similar growth tracks for all cases considered, however the parameter space investigated only represents a small region of possible parameters. More investigation is needed to ascertain the robustness of this variable. This could be an interesting source of analytic work.

These gas accretion rates were then implemented computationally along with the pebble accretion rates in order to explore the formation of gas giant planets. From simulation results, it was found that the core mass at crossover is an increasing function of stellar mass and a decreasing function of orbital radius, as expected. This suggests that planets forming close to high mass stars contain higher amounts of solid material, which may lead to higher metallicites. It was also seen that the gradients of the change of core mass at crossover over the conditions of stellar mass and of orbital radius change at different locations. The gradient over stellar mass is stronger at lower stellar masses and weaker at higher stellar masses, while the gradient over orbital radius is stronger at smaller separations and weaker at larger separations, which reflect the differences in pebble accretion rates.

The timescales to reach crossover mass, the onset of runaway gas accretion, were also investigated. It was found that the timescale to crossover is robustly within the estimated disk lifetime for planets forming around stars of approximately 0.5 solar masses or greater. The timescale stays robust across the range of orbital separations investigated. There is however a sharp increase in the timescales involved once we drop to stars of 0.2 solar masses, with the time to crossover extending beyond the average lifetime of a disk and increasing very strongly with orbital separation. This indicates a minimum stellar mass and orbital separation, below and beyond which a gas giant planet is not likely to form. We estimate the transition stellar mass value coarsely as 0.2 solar masses. Additionally, we noticed a correlation between the timescales to crossover and the total planet mass at the breakpoint value. There existed a sharp transition value between 0.2 and 0.5 solar masses. It was determined that planets which have a total mass of approximately 40 Earth masses or less at the breakpoint have timescales to crossover too long to reach crossover within the disk lifetime. It would be of useful further work to be able to predict the total planet mass at crossover, which gives an estimation into the timescale of growth, determining the success or failure of a forming gas giant.

There are some important physical effects which were not included in this investigation. Although it was found that the evolving disk cases follow the same growth tracks in the space of $\dot{M}_{\rm env}$ as a function of the variable $M_{\rm env}\,\dot{M}_z$, their investigation was not included in this study and is an important aspect of further work. The evolving disks were shown to have a considerable effect on the evolution of a gas giant planet. The solid accretion rates in the gas of evolving disks are not as strong as in the non-evolving case. This occurs due to a depletion of solid material over time. This leads to lower solid accretion rates, meaning lower total masses at crossover, lower gas accretion rates in general and conceivably a lower metallicity of a gas giant planet, given the lower core mass at crossover. In some cases, as in the cases of low mass stars, it is impossible for gas giant planets to form in the evolving case, since the disk depletes faster than solid material can be accreted. This actually leads to a *decrease* in the solid accretion rate over time, meaning that the gas accretion rates never become high enough to reach crossover mass. The rate at which the disk depletes can be investigated analytically though the equations presented in this study and are an important aspect of further investigation. In the gas accretion fitting function, it would be of particular importance to predict the breakpoint values for evolving disks, as well as other parameters.

Envelope enrichment was also not considered in this study. This acts to increase the fraction of solid material in the envelope, increasing the opacity but also the mass of the planet. The additional solid material in the envelope can either act to slow growth due to longer cooling times, or increase the gravitational strength of the planet leading to further accretion. These factors would influence the formation of a gas giant planet and would be useful in further work. Similarly, each simulation was performed at a single orbital radius with no orbital migration included. There are two types of orbital migration, namely type 1 and type 2 migration. Given that the investigations here are only to the crossover mass, the inclusion of type 1 orbital migration, stemming from resonances and interactions with the gas disk, would be of importance, since the solid accretion rates change significantly over orbital radius, influencing the growth tracks of the forming planets. Lastly, the breakpoint

ratio value between the envelope and total mass used in this investigation, 0.22, was found through trial and error, without any robust justification. Another ratio value may be more optimum, leading to more stable gas accretion rates, and would be the subject of further investigation. It was noted that the ratio between the gas accretion and solid accretion rates at this point were a little over unity. A more optimum value of the breakpoint may be better defined by the point where the ratio of accretion rates is equal to unity and would lead to a slightly smaller value of the ratio for the envelope mass to total mass. The idea of the critical core mass may also be used as a transition point, demarcating two growth regimes. Accurate models of critical core masses, similar to the work of Mizuno (1980) [25], given a certain orbital radius and stellar mass, could be developed and used as a breakpoint value.

From the discussion in the theory section on stellar classifications, we learned that the luminosity of an early star can be significantly higher than later values upon entry onto the main sequence after following the vertical Hayashi track on the H-R diagram. The formation of planets occurs very early on in the star's lifetime, meaning that it's luminosity value could change significantly during formation, affecting the temperature of the gas disk in turn. The temperature of the gas disk greatly affects solid accretion rates and, in turn, gas accretion rates and therefore the timescales of growth. A higher temperature leads to inhibited solid accretion rates, delaying the onset of significant gas accretion and therefore lengthening the timescale to crossover mass. The effects of evolving stellar luminosity should be included in evolution models if possible.

Lastly, the solid accretion rates investigated here only took into account pebble accretion. Although this can be a main source of solid accretion, it is inaccurate to assume that bodies large enough to avoid aerodynamic drag effects are either depleted from the vicinity of the forming planet or are not accounted for in the solid accretion rates. It would be useful to include the effects of planetesimal accretion and inspect how it affects the fitting functions and the validity of the variable $M_{\rm env}\,\dot{M}_z$.

A Pebble Accretion Model

The pebble accretion rates are taken from Lyra et al. (2023) [19] and are detailed here.

The solid accretion rate from pebble accretion is given as

$$\dot{M}_{\rm pe} = \pi R_{\rm acc}^2 \rho_{\rm pe} \delta v \exp(-\xi) \left[I_0(\xi) + I_1(\xi) \right] , \tag{89}$$

where

$$\xi = \left(\frac{R_{\rm acc}}{2 H_{\rm pe}} \right)^2 . \tag{90}$$

The relative velocity of particles is

$$\delta v = \Omega_K R_{\rm acc} , \tag{91}$$

and the the radius of accretion

$$R_{\rm acc} = \left(\frac{\rm St}{0.1} \right)^{1/3} R_H , \tag{92}$$

where St is the Stokes number and the Hill radius, R_H, is given as

$$R_H = a \left(\frac{M_{\rm planet}}{3 M_{\rm star}} \right)^{1/3} . \tag{93}$$

The density of pebbles can be computed as

$$\rho_{\rm pe} = \frac{\Sigma_{\rm pe}}{\sqrt{2\pi} H_{\rm pe}} , \tag{94}$$

where the pebble scale height is given as

$$H_{\rm pe} = H \sqrt{\frac{\alpha_T}{(\alpha_T + {\rm St})}} \tag{95}$$

where α_T is the turbulent alpha parameter, with the gas scale height

$$H = \frac{c_s}{\Omega} . \tag{96}$$

The pebble disk surface density is obtained from the continuity requirement

$$\Sigma_{\rm pe} = \frac{\dot{M}_{\rm pf}}{2\pi r v_{\rm R,pe}} , \tag{97}$$

with

$$\dot{M}_{\rm pf} = z \dot{M}_{\rm gas} . \tag{98}$$

The radial drift

$$v_{\rm R,pe} = -2\,{\rm St}\,\eta\; v_K + v_{\rm R,disk} \tag{99}$$

where

$$\eta = -\frac{1}{2}\left(\frac{H}{r}\right)^2 \frac{\partial \ln P}{\partial \ln r}\,, \tag{100}$$

where $\partial \ln P/\partial \ln r$ is the gradient of the disk pressure in log space, and the radial velocity of gas in the disk obtained from the continuity requirement

$$v_{\mathrm{R,disk}} = -\frac{\dot{M}_{\mathrm{gas}}}{2\pi r \Sigma_{\mathrm{gas}}}\,. \tag{101}$$

B Simulation Parameter Values

The values of model parameters used in the MESA simulations is presented here. Note that these values are common across all simulations.

Parameter	Value	Parameter	Value
k_B	1.380649×10^{-16} erg/K^{-1}	α	1×10^{-3}
μ	2.34	z	0.01
m_H	$1.66053906717 \times 10^{-24}$ g	St	0.01
$\dot{M}_{0,\mathrm{disk}}$	$1 \times 10^{-8}\,\mathrm{M}_\odot\,\mathrm{yr}^{-1}$	α_{T}	3.3×10^{-5}
r_{out}	50 AU	$\partial \ln P/\partial \ln r$	-2.7857
γ	15/14	t_0	8×10^5 yr

Table 10: Parameter values used in simulations of gas disks and solid accretion rates. The parameters correspond to the theory outlined for the disks and pebble accretion. The parameters here are constant over all simulations.

The outer boundary conditions for all cases considered can be obtained using the equations outlined in the thesis. The following table, however, shows the calculated values for convenience.

Star Mass [$M_\odot$]	Distance [AU]	T [K]	P [Ba]
1	3	93.669	0.4784
	5	75.251	0.1112
	7	65.145	0.04199
	9	58.4929	0.02013
	11	53.6723	0.01112
	12.87	50.179	0.00696
	4.23	80.843	0.17957
0.2	1.75	101.086	0.0967
	2.92	81.1712	0.0232
	4.09	70.256	0.009089
	5.26	63.075	0.00451
	6.43	57.873	0.002577
	7.31	54.777	0.0018
	3.12	78.8989	0.0193

Table 11: The outer boundary conditions for the simulation cases considered. The orbital radii 3 to 11 AU for the G-star and 1.75 to 6.43 AU for the M-star were used in the fitting procedure, while the remaining cases were used as tests to assess the quality of the fitting functions.

References

[1] Aleksander Wolszczan and Dail A Frail. A planetary system around the millisecond pulsar psr1257+ 12. *Nature*, 355(6356):145–147, 1992.

[2] Rodney Gomes, Harold F Levison, Kleomenis Tsiganis, and Alessandro Morbidelli. Origin of the cataclysmic late heavy bombardment period of the terrestrial planets. *Nature*, 435(7041):466–469, 2005.

[3] Francis LeBlanc. *An introduction to stellar astrophysics*. John Wiley & Sons, 2011.

[4] Tom Ray. Losing spin: the angular momentum problem. *Astronomy & Geophysics*, 53(5):5–19, 2012.

[5] Jonathan P Williams and Lucas A Cieza. Protoplanetary disks and their evolution. *Annual Review of Astronomy and Astrophysics*, 49(1):67–117, 2011.

[6] Jack J Lissauer. Planet formation. *In: Annual review of astronomy and astrophysics. Vol. 31 (A94-12726 02-90), p. 129-174.*, 31:129–174, 1993.

[7] Martin Asplund, Nicolas Grevesse, A Jacques Sauval, and Pat Scott. The chemical composition of the sun. *Annual review of astronomy and astrophysics*, 47(1):481–522, 2009.

[8] Philip J Armitage. *Astrophysics of planet formation*. Cambridge University Press, 2020.

[9] Nicolai Ivanovich Shakura and Rashid Alievich Sunyaev. Black holes in binary systems. observational appearance. *Astronomy and Astrophysics, Vol. 24, p. 337-355*, 24:337–355, 1973.

[10] Donald Lynden-Bell and Jim E Pringle. The evolution of viscous discs and the origin of the nebular variables. *Monthly Notices of the Royal Astronomical Society*, 168(3):603–637, 1974.

[11] James E Pringle. Accretion discs in astrophysics. *In: Annual review of astronomy and astrophysics. Volume 19.(A82-11551 02-90) Palo Alto, CA, Annual Reviews, Inc., 1981, p. 137-162.*, 19:137–162, 1981.

[12] JN Connelly, J Bollard, and M Bizzarro. Pb–pb chronometry and the early solar system. *Geochimica et Cosmochimica Acta*, 201:345–363, 2017.

[13] Peter Goldreich and William R Ward. The formation of planetesimals. *Astrophysical Journal, Vol. 183, pp. 1051-1062 (1973)*, 183:1051–1062, 1973.

[14] Andrew N Youdin and Jeremy Goodman. Streaming instabilities in protoplanetary disks. *The Astrophysical Journal*, 620(1):459, 2005.

[15] VS Safronov and EV Zvjagina. Relative sizes of the largest bodies during the accumulation of planets. *Icarus*, 10(1):109–115, 1969.

[16] Sebastian Lorek and Anders Johansen. Growing the seeds of pebble accretion through planetesimal accretion. *Astronomy & Astrophysics*, 666:A108, 2022.

[17] CW Ormel and HH Klahr. The effect of gas drag on the growth of protoplanets-analytical expressions for the accretion of small bodies in laminar disks. *Astronomy & Astrophysics*, 520:A43, 2010.

[18] Michiel Lambrechts and Anders Johansen. Rapid growth of gas-giant cores by pebble accretion. *Astronomy & Astrophysics*, 544:A32, 2012.

[19] Wladimir Lyra, Anders Johansen, Manuel H Cañas, and Chao-Chin Yang. An analytical theory for the growth from planetesimals to planets by polydisperse pebble accretion. *The Astrophysical Journal*, 946(2):60, 2023.

[20] Alan P Boss. Giant planet formation by gravitational instability. *Science*, 276(5320):1836–1839, 1997.

[21] Viktor Sergeevich Safronov. Evolution of the protoplanetary cloud and formation of the earth and the planets. *Israel Program for Scientific Translations, 1972*, 1972.

[22] Alar Toomre. On the gravitational stability of a disk of stars. *Astrophysical Journal, vol. 139, p. 1217-1238 (1964).*, 139:1217–1238, 1964.

[23] Ravit Helled, Peter Bodenheimer, Morris Podolak, Aaron Boley, Farzana Meru, Sergei Nayakshin, Jonathan J Fortney, Lucio Mayer, Yann Alibert, and Alan P Boss. Giant planet formation, evolution, and internal structure. *arXiv preprint arXiv:1311.1142*, 2013.

[24] Morris Podolak, William B Hubbard, and James B Pollack. Gaseous accretion and the formation of giant planets. In *Protostars and Planets III*, pages 1109–1147, 1993.

[25] Hiroshi Mizuno. Formation of the giant planets. *Progress of Theoretical Physics*, 64(2):544–557, 1980.

[26] Peter Bodenheimer and James B Pollack. Calculations of the accretion and evolution of giant planets: The effects of solid cores. *Icarus*, 67(3):391–408, 1986.

[27] David John Stevenson. Formation of the giant planets. *Planetary and Space Science*, 30(8):755–764, 1982.

[28] James B Pollack, Olenka Hubickyj, Peter Bodenheimer, Jack J Lissauer, Morris Podolak, and Yuval Greenzweig. Formation of the giant planets by concurrent accretion of solids and gas. *icarus*, 124(1):62–85, 1996.

[29] Masahiro Ikoma, Kiyoshi Nakazawa, and Hiroyuki Emori. Formation of giant planets: dependences on core accretion rate and grain opacity. *The Astrophysical Journal*, 537(2):1013, 2000.

[30] Ana-Maria A Piso and Andrew N Youdin. On the minimum core mass for giant planet formation at wide separations. *The Astrophysical Journal*, 786(1):21, 2014.

[31] Bertram Bitsch, Michiel Lambrechts, and Anders Johansen. The growth of planets by pebble accretion in evolving protoplanetary discs. *Astronomy & Astrophysics*, 582:A112, 2015.

[32] Steven W Stahler and Francesco Palla. *The formation of stars*. John Wiley & Sons, 2008.

[33] Cecilia Payne Gaposchkin. Annie jump cannon. *Science*, 93(2419):443–444, 1941.

[34] Bill Paxton, Lars Bildsten, Aaron Dotter, Falk Herwig, Pierre Lesaffre, and Frank Timmes. Modules for experiments in stellar astrophysics (mesa). *The Astrophysical Journal Supplement Series*, 192(1):3, 2010.

[35] Claudio Valletta and Ravit Helled. Giant planet formation models with a self-consistent treatment of the heavy elements. *The Astrophysical Journal*, 900(2):133, 2020.

[36] EI Chiang and P Goldreich. Spectral energy distributions of t tauri stars with passive circumstellar disks. *The Astrophysical Journal*, 490(1):368, 1997.

[37] Sean M Andrews, Katherine A Rosenfeld, Adam L Kraus, and David J Wilner. The mass dependence between protoplanetary disks and their stellar hosts. *The Astrophysical Journal*, 771(2):129, 2013.

[38] Brianna Zawadzki, Daniel Carrera, and Eric B Ford. Rapid formation of super-earths around low-mass stars. *Monthly Notices of the Royal Astronomical Society*, 503(1):1390–1406, 2021.

[39] Ronald W Schafer. What is a savitzky-golay filter?[lecture notes]. *IEEE Signal processing magazine*, 28(4):111–117, 2011.

[40] Linn EJ Eriksson, Marit AS Mol Lous, Sho Shibata, and Ravit Helled. Can uranus and neptune form concurrently via pebble, gas, and planetesimal accretion? *Monthly Notices of the Royal Astronomical Society*, 526(4):4860–4876, 2023.

[41] Benjamin J Fulton, Lee J Rosenthal, Lea A Hirsch, Howard Isaacson, Andrew W Howard, Cayla M Dedrick, Ilya A Sherstyuk, Sarah C Blunt, Erik A Petigura, Heather A Knutson, et al. California legacy survey. ii. occurrence of giant planets beyond the ice line. *The Astrophysical Journal Supplement Series*, 255(1):14, 2021.

[42] Basmah Riaz, Nicolas Lodieu, and John E Gizis. Brown dwarf disks at ages of 5–10 myr. *The Astrophysical Journal*, 705(2):1173, 2009.